The Astrophysical Journal, 850:15 (16pp), 2017 November 20 https://doi.org/10.3847/1538-4357/aa9021

Detection of Enhanced Central Mass-to-light Ratios in Low-mass Early-type Galaxies: Evidence for Black Holes?

Renuka Pechetti[1], Anil Seth[1], Michele Cappellari[2], Richard McDermid[3], Mark den Brok[4], Steffen Mieske[5], and Jay Strader[6]
[1] Department of Physics and Astronomy, University of Utah, 115 South 1400 East, Salt Lake City, UT 84112, USA
[2] Sub-department of Astrophysics, Department of Physics, University of Oxford, Denys Wilkinson Building, Keble Road, Oxford OX1 3RH, UK
[3] Department of Physics and Astronomy, Macquarie University, Sydney, NSW 2109, Australia
[4] ETH Zurich, Switzerland
[5] European Southern Observatory, Alonso de Cordova 3107, Vitacura, Santiago, Chile
[6] Center for Data Intensive and Time Domain Astronomy, Department of Physics and Astronomy, Michigan State University, 567 Wilson Road, East Lansing, MI 48824, USA
Received 2017 July 26; revised 2017 September 16; accepted 2017 September 24; published 2017 November 13

Abstract

We present dynamical measurements of the central mass-to-light ratio (M/L) of a sample of 27 low-mass early-type ATLAS^{3D} galaxies. We consider all ATLAS^{3D} galaxies with $9.7 < \log(M_\star/M_\odot) < 10.5$ in our analysis, selecting out galaxies with available high-resolution *Hubble Space Telescope* (*HST*) data, and eliminating galaxies with significant central color gradients or obvious dust features. We use the *HST* images to derive mass models for these galaxies and combine these with the central velocity dispersion values from ATLAS^{3D} data to obtain a central dynamical M/L estimate. These central dynamical M/Ls are higher than dynamical M/Ls derived at larger radii and stellar population estimates of the galaxy centers in ∼80% of galaxies, with a median enhancement of ∼14% and a statistical significance of 3.3σ. We show that the enhancement in the central M/L is best described either by the presence of black holes in these galaxies or by radial initial mass function variations. Assuming a black hole model, we derive black hole masses for the sample of galaxies. In two galaxies, NGC 4458 and NGC 4660, the data suggest significantly overmassive black holes, while in most others only upper limits are obtained. We also show that the level of M/L enhancements we see in these early-type galaxy nuclei are consistent with the larger enhancements seen in ultracompact dwarf galaxies (UCDs), supporting the scenario where massive UCDs are created by stripping galaxies of these masses.

Key words: galaxies: elliptical and lenticular, cD – galaxies: formation – galaxies: kinematics and dynamics – quasars: supermassive black holes

Supporting material: machine-readable tables

1. Introduction

Early-type galaxies (ETGs) include all elliptical (E) and lenticular (S0) galaxies that are characterized by old, red stellar populations. Massive ETGs contain very little gas and dust, have quenched their star formations, and typically host massive black holes (BHs) at their centers. The BH masses in these galaxies follow relatively tight scaling relationships with overall galaxy properties, suggesting that the BHs and galaxies have coevolved (e.g., Kormendy & Ho 2013).

In lower-mass ETGs ($3 \times 10^9 \lesssim M_\star/M_\odot \lesssim 4 \times 10^{10}$) there is also evidence that they host BHs at their centers: X-ray measurements show weak active galactic nuclei (AGNs) at the centers of many of these low-mass ETGs (Gallo et al. 2010; Miller et al. 2012). Miller et al. (2015) use these data to derive estimates for the BH occupation fraction and find that most galaxies with mass above $\sim 3 \times 10^9\ M_\odot$ do host massive BHs. However, very few BH mass measurements exist for these galaxies. The recent compilation of BH masses by Saglia et al. (2016) contains just 6 galaxies with velocity dispersions within the effective radius $\sigma_e \lesssim 100\ \mathrm{km\ s^{-1}}$, 2 ETGs with galaxy bulge masses below $3 \times 10^{10}\ M_\odot$, and 10 ETGs with galaxy dynamical masses below $\sim 3 \times 10^{10}\ M_\odot$ (Cappellari et al. 2013b). The lowest-mass ETGs with dynamical BH mass estimates have $M_\star \sim 10^9\ M_\odot$ (Verolme et al. 2002; van den Bosch & de Zeeuw 2010; Nguyen et al. 2017).

Using existing dynamical BH mass estimates, an empirical correlation is seen between the velocity dispersions and BH masses: the M–σ relationship (e.g., Magorrian et al. 1998; Gebhardt et al. 2000; Kormendy & Ho 2013; McConnell & Ma 2013; Saglia et al. 2016). Although this relationship is very well constrained at the high-mass end, fewer measurements exist at lower masses, due to the difficulty of measuring the small BHs expected in these galaxies. Läsker et al. (2016) and Greene et al. (2016) show that late-type galaxies with $\sigma \sim 100\ \mathrm{km\ s^{-1}}$ (similar to the Milky Way) and bulge masses of $\sim 10^{10}\ M_\odot$ show a large scatter in BH mass as measured from masers. This wide range of BH masses can also be interpreted as a steepening of the scaling relationships (Graham & Scott 2015; Savorgnan et al. 2016). No comparable sample of low-mass ETG BH mass measurements is available.

One promising new avenue for finding BHs in low-mass galaxies is the recent discovery of BHs in ultracompact dwarf galaxies (UCDs). UCDs are dense stellar systems with masses ranging from a few million to a hundred million solar masses and sizes <100 pc (e.g., Norris et al. 2014). UCDs, like ETGs, are typically found in denser environments. Integrated dispersion measurements of the UCDs revealed dynamical mass-to-light ratio (M/L) estimates higher than expected based on their stellar populations (e.g., Hąsegan et al. 2005; Mieske et al. 2013; see also Figure 1). Recently, using resolved kinematics of the UCDs, these enhanced M/Ls have been shown in a few cases to be due to the presence of supermassive BHs (Seth et al. 2014; Ahn et al. 2017). These BHs make up a high fraction of the mass of the UCDs (10%–20%), inflating the integrated dispersion

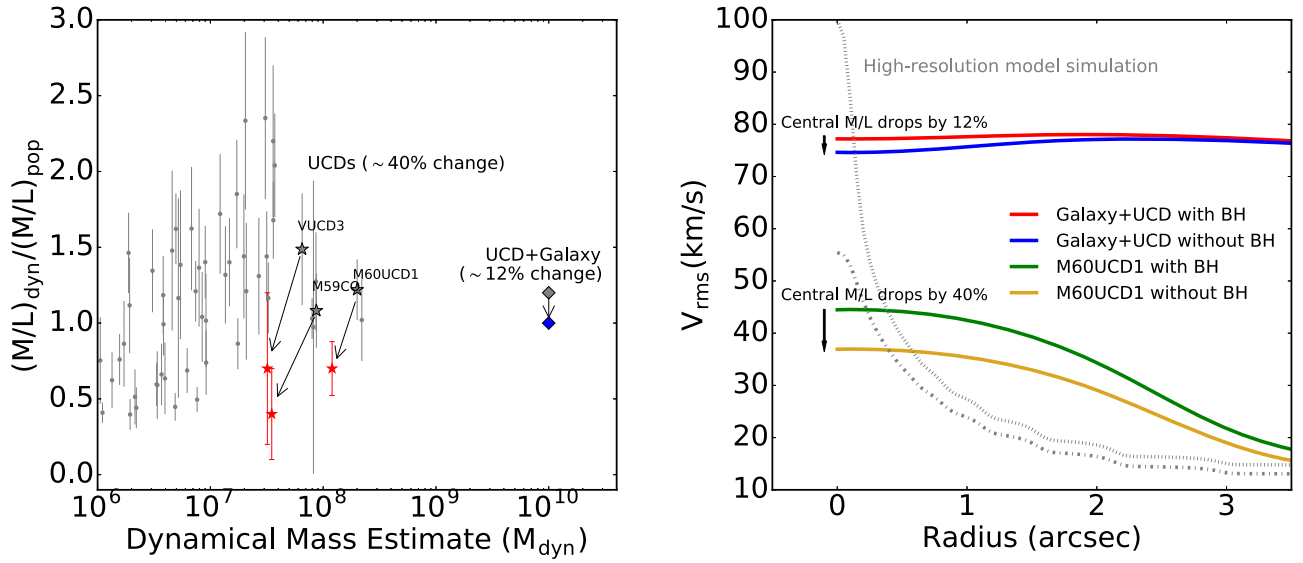

Figure 1. Left panel: gray circles are globular clusters and UCDs from Mieske et al. (2013). Elevation in the dynamical M/L ($(M/L)_{\rm dyn}$) is observed when compared to the stellar M/L ($(M/L)_{\rm pop}$). The stellar dynamical M/L drops for UCDs (in red) and the UCD+galaxy model (in blue) after including the dynamical effect of a BH. Right panel: simulated radial velocity dispersion profiles for M60-UCD1 with a PSF FWHM of 2″. The bottom profiles are for M60-UCD1 only, with (green) and without (yellow) a BH in it. The top profiles are when a galaxy is added around M60-UCD1 with (red) and without (blue) a BH in it. The gray lines show models with adaptive optics resolution for M60-UCD1 with (top gray profile) and without (bottom gray profile) a BH. Note the drop in the central dispersion between these high-resolution models and those simulated at ground-based resolution.

measurements. These high mass fraction BHs suggest that these UCDs are the tidally stripped remnants of once larger galaxies (likely ETGs). They also suggest that it might be possible to detect BHs in ETGs through enhancements in their central M/Ls, even at ground-based resolution.

Here, we analyze a sample of low-mass ETGs and derive accurate central M/Ls using high-resolution mass models. We compare these M/Ls to the dynamical M/Ls determined at larger radii and the central stellar M/Ls inferred from their stellar populations. In Section 2, we discuss the connection between ETGs and UCDs to set expectations for our study. Then, in Section 3 we discuss the selection of our sample of 27 ETGs from the ATLAS^{3D} survey. Section 4 describes the modeling of *Hubble Space Telescope* (*HST*) data, including the derivation of point-spread functions (PSFs), creating multi-Gaussian expansion (MGE) mass models for *HST* images and analyzing their color maps. Section 5 describes the derivation of central M/L for the galaxies using Jeans anisotropic modeling and various sources of errors associated with our models. In Section 6, we describe our results, focusing on the enhancement in M/L. We consider possible interpretations of this enhancement in Section 7, estimating BH masses and discussing the possibility of radially varying initial mass function (IMF) and the impact of anisotropy in the galaxies. We conclude in Section 8.

2. Early-type Galaxies in the Context of UCDs

To motivate the measurement of central M/Ls in ETGs, in this section we consider what the expected dynamical signature of the BHs found in UCDs would be in a typical ETG before they are stripped. As mentioned in the introduction, the dynamical M/Ls of UCDs are higher than expected from their stellar populations. More specifically, integrated dispersion measurements of UCDs have been used to calculate dynamical M/Ls ($(M/L)_{\rm dyn}$) under the assumption that the mass distribution traces the light distribution of the UCD. These are enhanced relative to the maximum estimate of their stellar population M/L ($(M/L)_{\rm pop}$) assuming a Chabrier IMF (Hşasegan et al. 2005; Dabringhausen et al. 2009, 2010; Frank et al. 2011; Mieske et al. 2013; Strader et al. 2013). The left panel of Figure 1 shows that the enhancement can be seen in a majority of UCDs with dynamical mass estimates above a few million solar masses that show $(M/L)_{\rm dyn}/(M/L)_{\rm pop} > 1$. Taking into account the measured BH masses in the three objects with adaptive optics measurements, we find that $(M/L)_{\rm dyn}/(M/L)_{\rm pop}$ of the stellar component decreases on average 40% relative to the integrated estimates without a BH in the recent discoveries like M60-UCD1 (1.222 → 0.7; Seth et al. 2014), VUCD3 (1.02 → 0.7), and M59CO (1.04 → 0.4; Ahn et al. 2017).

To examine the effect of the BH on the dispersion profiles of the UCDs, we take the measured stellar M/L of M60-UCD1 and its stellar mass model (Seth et al. 2014) to predict the dispersion profiles with and without a $2.5 \times 10^7\ M_\odot$ BH (right panel of Figure 1) using isotropic Jeans modeling, described further in Section 5.1. The original M60-UCD1 measurement was made with adaptive optics and thus has a resolution of ∼0.″2, but we use ground-based measurements (2″ FWHM and a pixel size of 0.″94) for our models, similar to those presented in this paper. As expected, the inclusion of a BH results in a significant difference of 17% in the central dispersion, even at this lower resolution. Note that in Figure 1 the low-resolution model central velocity dispersions are lower (green and yellow profiles) compared to M60-UCD1's observed dispersion (Strader et al. 2013). We also show models with and without a BH observed at adaptive optics resolution (gray profiles); the upper of these profiles closely matches the observed $V_{\rm rms}$ profile of M60-UCD1 by Seth et al. (2014).

Based on the BH mass and nuclear properties, Seth et al. (2014) suggest that M60-UCD1 had a progenitor galaxy of mass around $10^{10}\ M_\odot$ before it was stripped. To simulate what this progenitor would have looked like, we take the central Sérsic component (likely the former nuclear star cluster of the

galaxy; Pfeffer & Baumgardt 2013) and add a typical 10^{10} $M_{\odot}$ ETG around it with Sérsic index $n = 2$ and effective radius $R_{\rm eff} = 1.15$ kpc (e.g., Kormendy et al. 2009). We create a mass model from these two components and again use Jeans isotropic models to simulate the galaxy with and without a 2.5×10^7 $M_{\odot}$ BH. A smaller difference of 4.4% is seen in the central dispersion than in the "naked" UCD simulation, due to the mixing of galaxy light from larger radii. Thus, the dynamical effect of a BH is more visible in a stripped nucleus than it is in its original galaxy. When we translate the change in velocity dispersions to a change in M/L using our dynamical models, we find that the UCD model has a drop of ∼40% in central M/L when a BH is included, whereas the UCD+galaxy model has a drop of ∼10%–12% in central M/L when a BH is included in the model. We also ran a similar simulation for M59CO (Ahn et al. 2017) using a lower-mass galaxy, with similar results.

These simulations suggest that if comparable BHs to those found in UCDs are present in low-mass ETGs, they could inflate the inferred central M/Ls by ∼10% in ground-based resolution spectra, and thus may be detectable in existing data sets. This motivates the study of central M/L measurements presented here.

3. Data and Sample Selection

In this study, we combine central velocity dispersion values of the galaxies from the ATLAS^{3D} survey (Cappellari et al. 2011), with high-resolution mass models derived from *HST* images to obtain the central M/Ls of these galaxies. Here we discuss the ATLAS^{3D} data and the sample selection of galaxies from the ATLAS^{3D} survey with existing *HST* archival data.

3.1. ATLAS^{3D} *Spectra*

We use the optical integral field spectroscopic observations for the ATLAS^{3D} galaxies taken from SAURON Integral Field Unit (IFU) on the William Herschel Telescope (WHT). The SAURON IFU (Bacon et al. 2001) has a spatial sampling of $0\farcs94$ pixel^{-1} in a low-resolution mode with a spectral window of 4810–5350 Å. The ATLAS^{3D} team has used the resulting 3D data cubes to derive kinematic measurements of galaxies (Cappellari et al. 2011).[7] We use two data products from ATLAS^{3D}: (1) the central velocity dispersions of the galaxies and (2) the fluxes of the spectra to fit the PSF of the ATLAS^{3D} data.

For one galaxy, NGC 4342, ATLAS^{3D} data were taken under poor conditions, resulting in less reliable data, so we use data from van den Bosch et al. (1998) for this galaxy. Its spectra are from WHT, and the resolution is ∼1″, similar to ATLAS^{3D} data.

3.2. *Sample Selection from* ATLAS^{3D} *Galaxies*

The ATLAS^{3D} project is a multiwavelength survey combined with numerical simulations and theoretical modeling of galaxy formation for 260 ETGs. These are selected to be within a volume of 1.16×10^5 Mpc^3 and a radius of 42 Mpc consisting of morphology of ellipticals (E-type) and S0 galaxies. Detailed selection criteria for these 260 galaxies, which are a complete and representative sample of the nearby ETG population, are described in Cappellari et al. (2011).

[7] Available from http://purl.org/atlas3d.

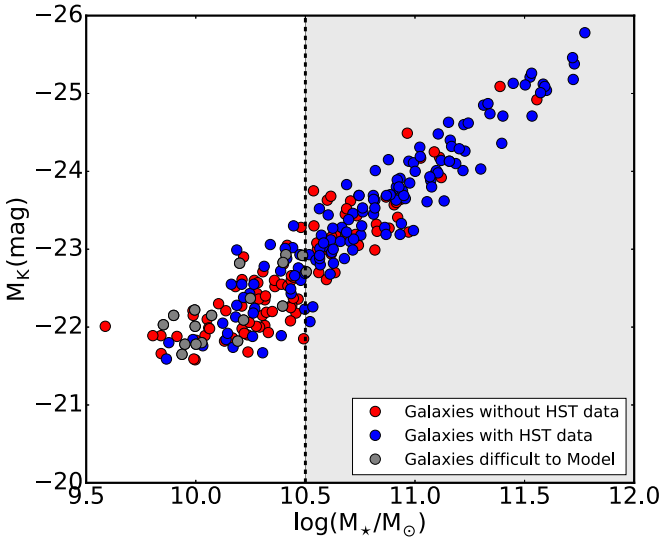

Figure 2. ATLAS^{3D} galaxy sample (Cappellari et al. 2011). Our selected low-mass ETG sample has log$M_\star < 10.5$ $M_\odot$. The $M_\star$ is the total stellar mass measurement obtained by multiplying the total luminosity of the galaxy with the stellar M/L determined dynamically within ∼1 effective radius (R_e) (Table 1 of Cappellari et al. 2013b). The galaxies colored in blue have *HST* data, and those colored in red do not have *HST* data. Gray points are galaxies that had visible dust lanes or saturated pixels and were difficult to model, and thus were removed from our analysis.

This paper focuses on the lowest-mass portion of the sample of galaxies from the ATLAS^{3D} survey, as existing BH demographic studies include very few ETGs in this mass range. The ATLAS^{3D} galaxies were selected to have $M_K < -21.5$ mag (log$M_\star \gtrsim 9.7$ $M_\odot$), which sets the lower mass limit of the sample. We then make an upper mass cut at a dynamical mass of log$M_\star < 10.5$ $M_\odot$ to select the low-mass galaxies; this gives us 115 galaxies, of which we analyze only a subsample (see Figure 2).

3.3. *Sample Selection from* HST *Survey*

To create accurate mass models for measuring a central dynamical M/L, we require imaging data at higher resolution than the kinematics. We therefore selected only those galaxies that had archival *HST* data for the ETGs. We downloaded the *HST* imaging using the Hubble Legacy Archive,[8] including imaging from the Wide Field and Planetary Camera 2 (WFPC2), Advanced Camera for Survey (ACS)/Wide Field Channel (WFC), ACS/High Resolution Camera (HRC), and Wide Field Camera 3 (WFC3)/ultraviolet and visible light (UVIS).

To accurately model the light emitted from a galaxy, we used data only from filters with central wavelengths ⩾4739 Å/F475W. This minimizes any uncertainties due to dust and stellar population variations. From the *HST* data, we found a total of 55 out of 115 galaxies that had usable data in the preferred wavelengths. By visual inspection of these 55 galaxies, we discarded those that had noticeable dust lanes or saturated pixels at the center, as they would be difficult to model, leaving us with 35 galaxies. We then performed an analysis of color gradients of the galaxies to identify color variations at their centers, as described in Section 4.3. Those with large color variations were discarded from the sample. This left us with a sample of 27

[8] Available from https://hla.stsci.edu.

galaxies in which we can determine the accurate central M/Ls. Figure 2 shows our sample selection from ATLAS^{3D} and *HST* data, including the galaxies that were discarded. A complete list of these 27 galaxies that were used for modeling is available in the Appendix.

4. Creating High-resolution Mass Models

By focusing on galaxies with existing high-resolution *HST* archival data, we can create the mass models needed to obtain accurate central M/Ls. We create these using an MGE model (Emsellem et al. 1994; Cappellari 2002). In this section, we first discuss how we determine the *HST* PSFs to enable us to deconvolve our mass models. The construction of these mass models is then described. We also discuss the effects of color gradients at centers of the galaxies and how they affect our mass models.

4.1. Determining PSF of the HST Images

PSF modeling is important for our data, as we are focusing on the central arcsecond of the image, where its effects are significant, even at *HST* resolution. We derived $3'' \times 3''$ PSFs for *HST* images at the location of the galaxy nuclei using the `Tiny Tim` PSF modeling tool (Krist et al. 2011), assuming a blackbody of 4000 K. For each object, an undistorted PSF was generated using the appropriate camera and filter. For the ACS/WFC camera, we convolved a charge diffusion kernel corresponding to each filter; for the WFPC2/PC camera charge diffusion was not significant, and so no correction was made. For WFC3/UVIS, we used a distorted PSF from `Tiny Tim` that accounts for the charge diffusion kernel. We then fit these PSFs using the `mge_fit_sectors` code (Cappellari 2002), which is a 2D MGE model (Bendinelli 1991) and decomposes the image into a series of 2D Gaussians. The MGEs of the PSFs were forced to be circular, as our dynamical modeling code can only use symmetric PSFs. The PSF MGEs were then used in the creation of the mass models of the galaxies.

To test the sensitivity of our mass models to the PSF, we also remade our mass models using an empirical PSF for galaxies with ACS/WFC data. It was derived using stars in an ACS/WFC image. We found that our final derived M/L values are not sensitive to the exact PSF model we use, with $<1\%$ differences. This is small relative to the M/L errors from other sources, described in Section 5.2.

4.2. Surface Photometry Using MGEs

To parameterize the stellar mass distribution of the galaxy at high resolution, we used our *HST* data to build a mass model for the galaxy. We built the mass models using an MGE decomposition python code and fitting method described by Cappellari (2002). We used the code to first find the galaxy's center and its orientation in the image, and then we used the information to divide the galaxy into equally spaced sectors in eccentric anomaly. Using these sectors, Gaussians consisting of various widths were fit to a set of galaxy surface brightness measurements that were calculated along those sectors. The MGE galaxy model was then fit including convolution of the PSF MGE discussed in the previous section. The best-fit MGEs can then be deprojected to obtain a 3D luminosity model.

In nearby galaxies, sky subtraction in drizzled images often results in significant oversubtraction, as the sky regions contain

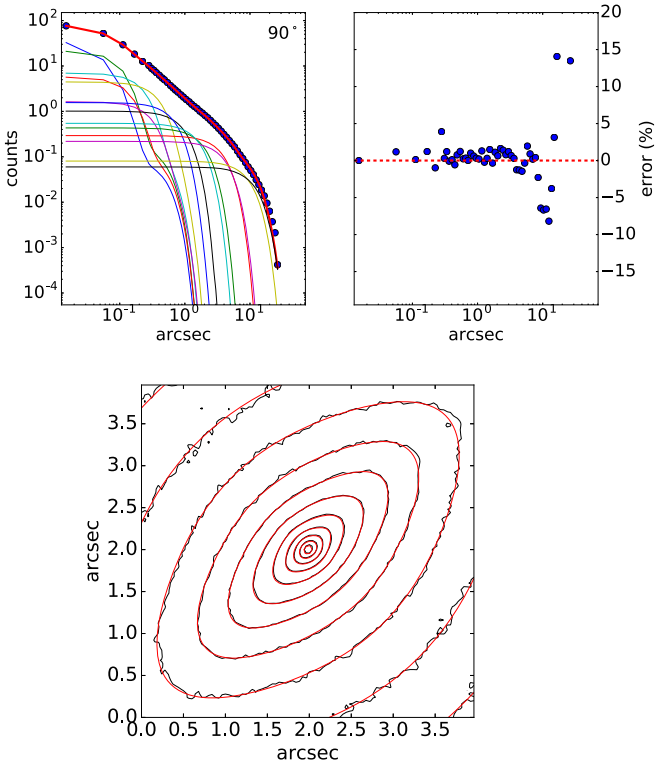

Figure 3. Top panel: comparison between the WFC3/UVIS photometry of NGC 3522 in F814W (blue circles) and the corresponding best-fit MGE model with 14 Gaussians (solid lines), along with the residuals in the right panel. Bottom panel: surface brightness contours of the central $4'' \times 4''$ of the same galaxy (black), with the MGE model overlaid in red.

a significant amount of galaxy light. Therefore, we add back the subtracted sky to the image of the galaxy. This leaves some low level of sky in the image, but this level is insignificant compared to the surface brightness at the centers of our galaxies. We also exclude the pixels in the image where there are no data. The MGEs were fit typically over an area of $25'' \times 25''$. A typical example of MGE fit to the surface brightness is shown in Figure 3. The derived MGE parameters of the same galaxy are given in Table 1, which describes the luminosity, width, and axis ratio (q) of each Gaussian.

All derived MGE profiles of the galaxies are available in the online version of Table 1. The MGEs are used in deriving M/L of the galaxies via dynamical modeling. Given the lack of color gradients and dust in most of our galaxies, we assume that the stellar mass follows the stellar light; we examine this assumption in greater detail in the next subsection.

4.3. Determining Color Profiles of the Galaxies

ETGs are often assumed to have uniformly old populations with little gas and dust (Thomas et al. 2005); however, especially low mass ETGs are observed to have some stellar population gradients (e.g., Rose et al. 2005; Goddard et al. 2017). Because our determination of central M/Ls depends critically on the assumption that mass traces light near the center of the galaxy, we check whether there are indications of dust or color gradients in our sample using color maps for the 27 out of 35 galaxies with data available in more than one *HST* filter.

Table 1
Multi-Gaussian Expansion Parameters of All 27 Galaxies

Galaxy	Filter	log$I$ ($L_\odot$ pc^{-2})	logσ (arcsec)	q
…	…	…	…	…
NGC 3522	F814W	5.486	−1.478	0.63
…	…	4.709	−0.861	0.55
…	…	4.184	−0.518	0.56
…	…	3.558	−0.211	0.72
…	…	3.804	0.096	0.32
…	…	3.236	0.132	0.79
…	…	3.266	0.228	0.37
…	…	3.028	0.539	0.66
…	…	2.545	1.069	0.50
…	…	…	…	…

Note. The parameters are the luminosity (I), width (σ), and axis ratio (q) of each Gaussian for NGC 3522. Only a portion of this table is shown here to demonstrate its form and content.

(This table is available in its entirety in machine-readable form.)

In this section, we quantify the color gradients in our galaxies and examine the effects they have on our central dynamical M/L estimates. Our central dispersion estimates from ATLAS^{3D} are taken using 0.″94 pixels under seeing conditions of $\sim$2″. Therefore, we are primarily concerned with color gradients within the central $\sim$1″ of the galaxy. If such color gradients exist, it would violate the assumption we are making that the M/L is constant over the region in which we fit the kinematics.

To create color maps for our sample galaxies, we used F555W and F814W filters for WFPC2/PC data, F475W and F850LP filters for ACS/WFC data, and F475W and F814W filters for WFC3/UVIS data. To remove the PSF effects in color maps, we cross-convolved the images in one filter with the PSF of the other filter before making our color maps. Example color maps for two galaxies in our sample are shown in the top panel of Figure 4. We calculated the color difference between the value measured at the center (within a circle of $R = 0.''05$) and that within a circular annulus of radius $R = 1''$ and width 0.″05 for all the galaxies in our sample to quantify their color gradients. By visual examination, we found this difference in colors to be a good indicator of significant color variation in the galaxy nucleus. The bottom panel of Figure 4 shows this color difference for all galaxies with available color maps; for simplicity we plot the different cameras/color differences on a single plot.

We exclude galaxies with large color differences in the central 1″ because dynamical modeling would lead to inaccurate estimation of their M/Ls. For example, if a galaxy is redder at the center than at 1″, we will underestimate the relative amount of mass at the center, and this will lead to an overestimation of the dynamical M/L. To quantify this effect, we alter our MGE models to find the error in M/L corresponding to a color gradient in the central 1″. We took our MGE models and varied the M/L of each individual component using the color–M/L relation of Bruzual & Charlot (2003). We converted the constant mass-follows-light profile to a changing mass profile based on the color of the galaxy. We found that for color gradients of 0.1 mag (in F555W–F814W, where the color corresponds to the largest difference in stellar M/L), our best-fit dynamical M/Ls vary by 3%–4%. This error

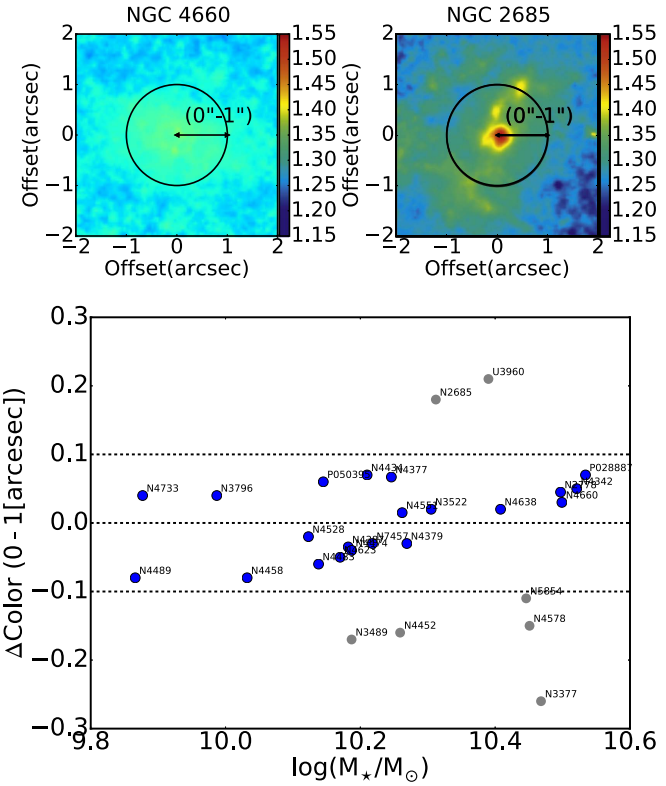

Figure 4. Color gradients in our low-mass ETG sample galaxies. Top left panel: color map (F555W–F814W) of central 1″ region of WFPC2/PC image of NGC 4660, which shows a minimal color gradient within the central 1″. Top right panel: color map (F555W–F814W) of NGC 2685, which shows a significant central color gradient. Bottom panel: color difference in the central 1” of the full sample of galaxies is calculated and plotted. We note that each galaxy in gray has color gradient >0.1 mag at its center; these galaxies have been excluded from most additional analysis, due to the lack of reliability in the central M/L estimates created by these central color gradients.

is comparable to the contribution of the dispersion error to our dynamical M/Ls, and therefore we remove all galaxies with color gradients more than 0.1 mag from the quantitative analysis presented in later sections.

For galaxies without color information, we examined their spectra for emission-line contribution, as this could also result in inaccurate mass profiles. From this examination, we removed NGC 5173, as it had significant emission-line flux in its ATLAS^{3D} spectra. The remainder of the sample of 27 galaxies (22 with color maps and 5 without color maps) is used for deriving the M/L using dynamical models.

4.4. Outer to Central Stellar Population Variations

In assessing our central M/Ls, we compare our dynamical M/Ls of the galaxy nuclei to those derived while fitting the full SAURON field of view (FOV), which extends to a typical radius of about $1R_e$ (Cappellari et al. 2013a). Here we explore the variations we expect owing to stellar population differences.

In low-mass ETGs, there can be populations of stars of various ages (e.g., McDermid et al. 2015). These stellar population variations can lead to M/L gradients within a galaxy. To quantify the size of those variations in our sample, we compare the stellar population M/L outside the nucleus within $1R_e$ ($(M/L)^{\rm out}_{\rm pop}$) with the central stellar population

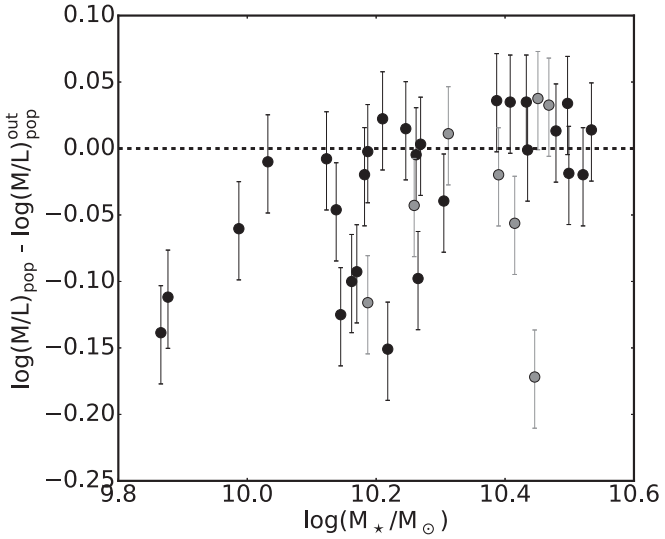

Figure 5. Ratio between $(M/L)_{\rm pop}$ (central stellar M/L) and $(M/L)^{\rm out}_{\rm pop}$ (outer stellar M/L; within $1R_e$) estimated from stellar population synthesis modeling as described in McDermid et al. (2015). Galaxies in gray are those with identified color gradients within $1''$. Negative values indicate lower M/Ls at the center.

mass-to-light ratio ($(M/L)_{\rm pop}$). We calculated the $(M/L)^{\rm out}_{\rm pop}$ by fitting the full observed spectra using a linear combination of single stellar population (SSP) synthetic spectra that were created assuming a Salpeter IMF, as explained in more detail in McDermid et al. (2015). The central $(M/L)_{\rm pop}$ values were derived by fitting only the central spectrum of the ATLAS$^{\rm 3D}$ SAURON field in an identical way to that presented in McDermid et al. (2015).

Figure 5 shows the plot of the ratio between $(M/L)_{\rm pop}$ and $(M/L)^{\rm out}_{\rm pop}$. We note that we calculated these values assuming both a Salpeter IMF (Salpeter 1955) and a Kroupa IMF (Kroupa 2001); the Salpeter IMF is used for comparison to $(M/L)^{\rm out}_{\rm pop}$ for consistency, but the Kroupa $(M/L)_{\rm pop}$ values will be used later in the paper. For most galaxies, the M/L at the center of the galaxy is lower than that in the outer parts of the galaxy, by as much as -0.15 dex. This suggests that most low-mass ETGs have younger stellar populations concentrated toward their centers. This is in agreement with the difference in the mass-weighted ages from spectral fits (McDermid et al. 2015). At the higher-mass end ($\log M_\star > 10.2$), some galaxies have higher central M/Ls, but the increase is always <0.04 dex. This suggests that, based purely on stellar population differences, we would expect the dynamical M/Ls at the center to typically be lower than the dynamical M/L at larger radii. We will return to this result when we compare our central and outer dynamical M/L values in Section 6.

5. Dynamical Modeling

In this section, we present the estimation of the central dynamical M/L of our sample galaxies. These central M/Ls are determined using dynamical models that scale the mass models to match the measured central dispersion values from ATLAS$^{\rm 3D}$. We also discuss the corresponding errors and their detailed analysis.

5.1. Determining Central M/Ls with Jeans Anisotropic Models

To create a dynamical model for comparing the central velocity dispersion, we use Jeans Anisotropic Models[9] (python version JAM; Cappellari 2008). As an input, the models require a mass model parameterized as an MGE. In brief, the JAM code constructs a 3D density profile by deprojecting the 2D MGE parameters. A gravitational potential is then generated based on the density profile. A BH can be added to this potential and is represented as a small Gaussian component. Even though a Keplerian potential can be used to describe the BH, it is easier and more efficient to model it as a Gaussian with a width smaller than those used for the galaxy components (Emsellem et al. 1994; (FWHM of BH)/(FWHM of PSF) $\sim$ 0.015). The Jeans' equations are then solved using the MGE models, and the predicted model kinematics are analytically integrated along the line of sight. They are then convolved with the PSF for comparison to the observed galaxy kinematics.

To obtain the best-fit central dynamical M/L $\{(M/L)_{\rm cen}\}$, we ran JAM models on the central pixel of the galaxies assuming a no-BH model for our sample of galaxies. We did not include any dark matter component, as the fraction of dark matter at the centers of galaxies is observed to be low (see Section 6). JAM models require a kinematic PSF and a pixel scale as an input. We use a pixel size of $0\farcs94$, which was the original scale of the SAURON data cube. We derived kinematic PSFs for all the galaxies by comparing the SAURON intensity with that of the model MGE images that were convolved with a circular Gaussian distribution. We then minimized the differences between those images and obtained the PSF width. Based on this method, we found PSFs' FWHM ranging from $1''$ to $3''$ with a median of $2''$.

To examine the effects of inaccurate PSF determinations, we performed tests by varying the sizes of PSFs from $1''$ to $3''$ FWHM. The change in the derived $(M/L)_{\rm cen}$ due to these PSF variations was found to be around 1%, which is small compared to the errors on the M/L from other sources, and in particular small compared to the expected BH effect (10%–15%). We also tested whether offsets of the galaxy kinematic data within the central pixel could cause significant errors in our M/L estimates. The median and maximum differences when evaluating our off-center by up to a half pixel were 0.2% and 1.8%, respectively, which is again very low compared to our overall errors.

Inclination and anisotropies are required as an input to the JAM models. Since these parameters for a galaxy cannot be found when only a single pixel is modeled, we used the anisotropies[10] and inclinations for the galaxies in our models from Table 1 of Cappellari et al. (2013b), which were derived using the full FOV, excluding the central $2''$.

To compare all the $(M/L)_{\rm cen}$ in a single filter, and for consistency with previous ATLAS$^{\rm 3D}$ measurements, we converted all our derived M/L values to Sloan Digital Sky Survey (SDSS) r-band values. This conversion was done in two ways: (1) for 22 galaxies with *HST* color information, we used the *HST* colors and magnitudes to estimate the r-band luminosity using conversions from Padova SSP models assuming solar metallicity (Bressan et al. 2012);[11] (2) for 5 galaxies that did not have color information, 10 Gyr SSP

[9] Available from http://purl.org/cappellari/software.
[10] Available from http://purl.org/atlas3d.
[11] Available from http://stev.oapd.inaf.it/cgi-bin/cmd.

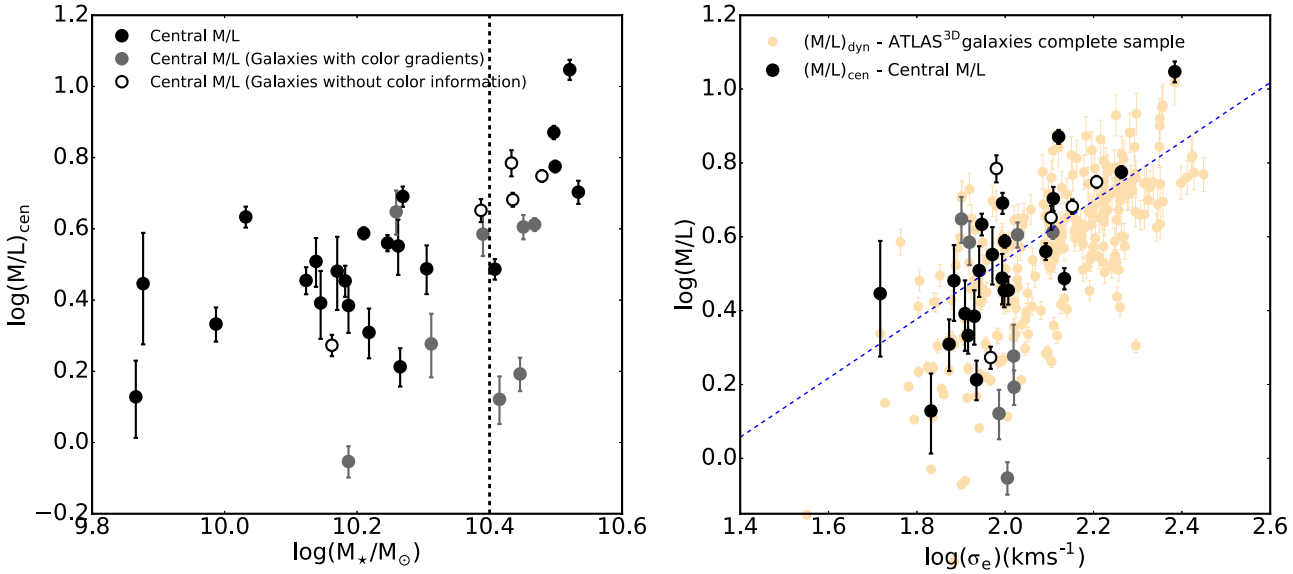

Figure 6. Left: best-fit central $(M/L)_{\rm cen}$ in r band derived from JAM modeling of the galaxy sample for a no-BH model, plotted against stellar dynamical mass of the galaxy. The error bars are from the errors on central velocity dispersion translated into M/L errors. Galaxies in gray have color gradients within the central $1''$. Galaxies with open circles do not have color information. Right: best-fit central $(M/L)_{\rm cen}$ in r band (in black, gray, and open circles) and $(M/L)_{\rm dyn}$ (in orange) from Cappellari et al. (2013a), which were derived using a similar method, plotted against effective velocity dispersion. The blue dashed line gives the global relation from Figure 17 of Cappellari (2016).

models were used to convert the *HST* magnitudes to r-band luminosity. Note that these converted *HST* fluxes lie within 1% of the fluxes from SDSS r-band images.

A plot of derived $(M/L)_{\rm cen}$ is shown in Figure 6. The left panel shows $(M/L)_{\rm cen}$ plotted against the total stellar galaxy mass ($M_\star$; defined in Figure 1). The right panel shows the $(M/L)_{\rm cen}$ plotted against the effective stellar velocity dispersion of the galaxy. The $(M/L)_{\rm dyn}$ (in orange; fitted within $\sim 1R_e$) are taken from Cappellari (2016). The dashed line shows the Cappellari (2016) global relation between r-band $(M/L)_{\rm dyn}$ and the velocity dispersion within one effective radius, σ_e, of the galaxy: $(M/L)_{\rm dyn} = 6 \times (\sigma_e/200\ {\rm km\ s^{-1}})$.

The distances and extinction values that are required for the JAM models were obtained from Table 3 of Cappellari et al. (2011). The distances to these galaxies range from 11 to 41 Mpc, with a median of 16.5 Mpc. The extinction values are in A_b mag. We converted all of these values into corresponding values in various filters by using extinction ratios from the Padova model website.

5.2. Sources of Error on $(M/L)_{\rm cen}$

In this section, we look at different sources of error in deriving our $(M/L)_{\rm cen}$ values, including both intrinsic and systematic errors. Above, we have already considered several sources of error (miscentering of the galaxy, misestimation of the SAURON PSF, etc.) and found these to be at the $\sim$1% level. Here, we consider the two main sources of error in the $(M/L)_{\rm cen}$ estimates of our sample galaxies:

1. Uncertainties in the central velocity dispersion of galaxies from SAURON data.
2. Systematic errors that include instrumental effects, PSF effects, and errors from JAM modeling.

The uncertainties in central velocity dispersion are easy to handle, as they can be directly included in modeling to derive the error limits on $(M/L)_{\rm cen}$. These errors, which form the major constituent of the errors in our data, range from 2 to 9 km s^{-1}on the central velocity dispersion of the galaxies, corresponding to fractional dispersion errors from 2% to 15%. We calculate the 1σ error in M/L by adding and subtracting the 1σ error on central velocity dispersion in our JAM models; this is then translated to an error on the best-fit M/L. The errors on our inferred log $(M/L)_{\rm cen}$, from the velocity dispersion errors, range from 0.012 to 0.14 dex (3%–38%).

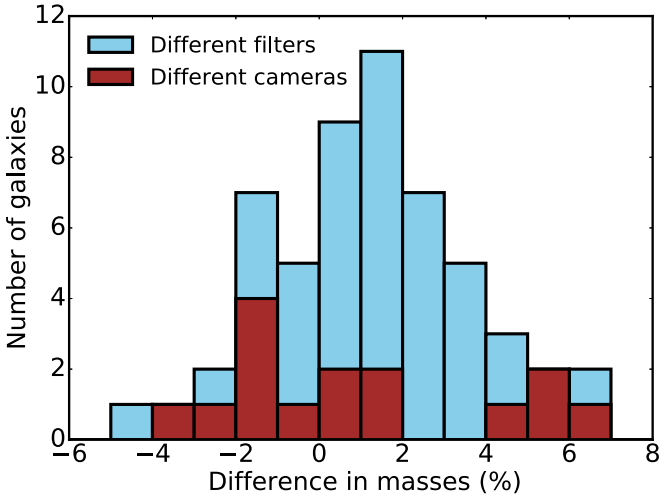

Figure 7. Histogram of systematic errors due to uncertainties in the mass models. The masses for each galaxy within the central $1''$ are calculated using mass models created from two different filters (on the same camera; shown in blue) or two different cameras (shown in red). The total histogram is best fit by a Gaussian with a standard deviation of 2.53% and a mean of 1.09%; we add this error to the errors due to dispersion in calculating our $(M/L)_{\rm cen}$ errors.

For our $(M/L)_{\rm cen}$ measurements, the dominant systematic error comes from errors in our mass models. We derive these errors by determining $(M/L)_{\rm cen}$ for a galaxy (using the method described in Sections 4 and 5) in two different *HST* filters observed with the same camera and then calculate the difference

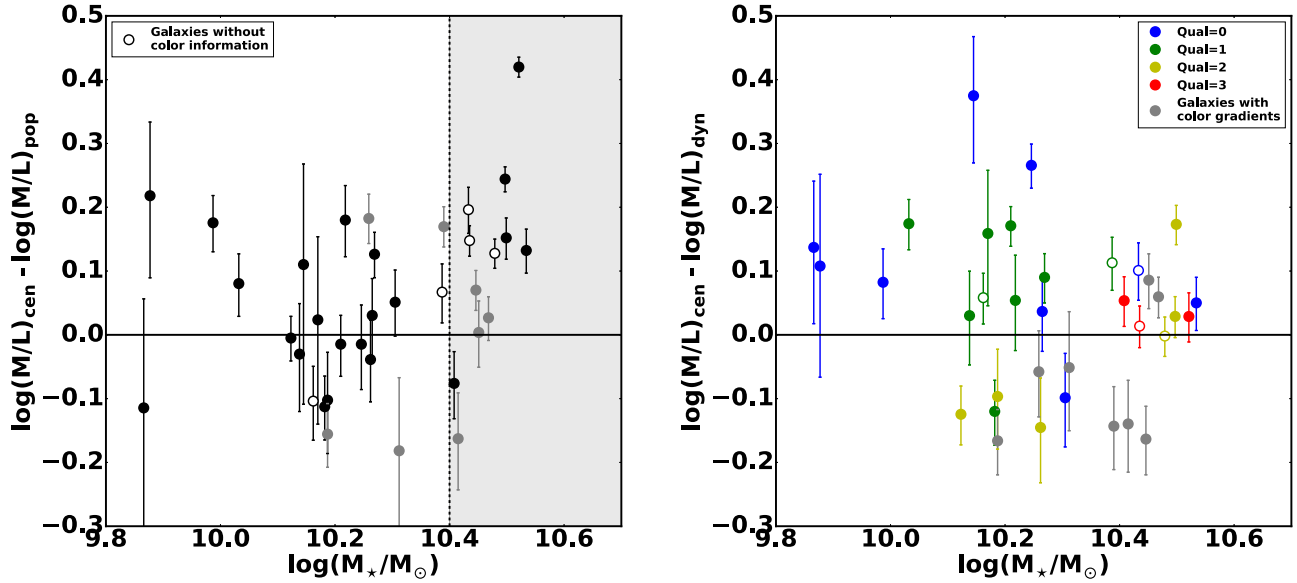

Figure 8. Central M/Ls of low-mass ETGs are typically higher than expected. Left panel: ratio of central $(M/L)_{\rm cen}$ and $(M/L)_{\rm pop}$ in r band (derived from stellar population models assuming a Kroupa IMF) plotted against the stellar mass of the galaxy. Galaxies above log$M_\star$ of 10.4 (gray region) appear to have systematically higher $(M/L)_{\rm cen}$ relative to $(M/L)_{\rm pop}$, perhaps due to global IMF variations. Right panel: ratio of central $(M/L)_{\rm cen}$ and $(M/L)_{\rm dyn}$ in r band (derived from dynamical models fit outside the nucleus and within $\sim 1R_e$) plotted against the mass of the galaxy. The galaxies are colored according to the quality of the fit of models for deriving $(M/L)_{\rm dyn}$ (Cappellari et al. 2013b). Qual = 0 indicates a low-quality JAM fit that is due to barred galaxies, dust, or uncertain deprojection due to a low inclination of the galaxy. Qual = 3 indicates a good JAM fit to the data. The galaxies that had a color gradient in central 0.″94 are indicated in gray, as their $(M/L)_{\rm cen}$ values are likely less reliable. The error bars include both errors from velocity dispersion measurements and mass-modeling errors.

in mass derived in the central arcsecond from the two filters. We also compare independent mass models derived from data in two different cameras, but with similar filters. For an object with a uniform color (i.e., after excluding the objects with dust lanes or significant color gradients), the mass models of a galaxy derived from two different filters should be identical. Mass models in two different cameras with the same filter should be identical regardless of the sample. However, misestimates in the PSF, residuals in the modeling, and random sampling errors of the surface brightness profile can lead to differences in these mass models. We can characterize the size of the systematic errors due to these by comparing the two filter and two camera models. The differences in these models are shown in Figure 7. We represent this model as a Gaussian error with standard deviation of 2.5% to match the width of this distribution and consider it as the systematic error throughout the paper.

To summarize, our major sources of error on our $(M/L)_{\rm cen}$ estimates are as follows:

1. Uncertainties from central velocity dispersion: 3%–38%.
2. Systematic mass-modeling errors: 2.5%.

6. Results: Enhancement in the Central Dynamical *M/L*

In the previous sections, we described the derivation of our mass models and corresponding determination of central, dynamical $(M/L)_{\rm cen}$ for our 27 low-mass ETGs. In the following, we compare the derived $(M/L)_{\rm cen}$ for the *HST* images with the M/Ls derived from stellar population estimates of the nuclear spectra ($(M/L)_{\rm pop}$) and dynamical M/L derived outside the nucleus ($(M/L)_{\rm dyn}$).

As discussed in Section 4.4, the $(M/L)_{\rm pop}$ was derived by fitting the central ATLAS$^{\rm 3D}$ spectrum to SSP models (McDermid et al. 2015). For the comparison to $(M/L)_{\rm cen}$ we use fits done with a Kroupa IMF, as these lower-mass ETGs are expected to have an IMF similar to Kroupa (Cappellari et al. 2012). The $(M/L)_{\rm dyn}$ was derived by dynamically modeling the 2D ATLAS$^{\rm 3D}$ kinematics at radii beyond 2″ using JAM models (Cappellari et al. 2013a, 2013b). These dynamical models exclude the central regions (<2″) of the galaxy owing to a possible bias from supermassive BHs being at their centers. The stellar and dark matter components were fit separately in the models (Model B of Cappellari et al. 2013b). For the $(M/L)_{\rm dyn}$, the best-fit models were used to predict the total dynamical mass at the center, including adding in the best-fit dark matter profile. This dark matter component makes up only 2%–3% of the central mass in our sample galaxies. The $(M/L)_{\rm dyn}$ is therefore the prediction for what we should observe for $(M/L)_{\rm cen}$ based on the dynamical model fits to the outer parts of each galaxy.

A comparison of $(M/L)_{\rm pop}$ and $(M/L)_{\rm dyn}$ with $(M/L)_{\rm cen}$ is shown in Figure 8 plotted against the galaxy stellar mass. We find that $(M/L)_{\rm cen}$ is larger than $(M/L)_{\rm dyn}$ in 21 of 27 galaxies and larger than $(M/L)_{\rm pop}$ in 17 of 27 galaxies. A trend is also seen in the left panel for galaxies that are massive (log $(M_\star/M_\odot) > 10.4$). Their high M/Ls as compared to $(M/L)_{\rm pop}$ (but not $(M/L)_{\rm dyn}$) may be due to systematic IMF variations observed using similar dynamical approaches in ETGs (Cappellari et al. 2012, 2013a; Posacki et al. 2015) and in the general galaxy population (Li et al. 2017). The galaxies with significant central color gradients (which can result in biased values of $(M/L)_{\rm cen}$) are shown in gray in these plots but are excluded from our analysis hereafter.

Due to the offset from stellar population values at the higher-mass end, we focus on the comparison between $(M/L)_{\rm cen}$ and $(M/L)_{\rm dyn}$ as shown in the right panel of Figure 8. We highlight the significance of the differences between $(M/L)_{\rm cen}$ and $(M/L)_{\rm dyn}$ in Figure 9; both panels show the clear offset toward higher values for $(M/L)_{\rm cen}$ relative to $(M/L)_{\rm dyn}$. The left panel shows a median offset of 14%. Assuming a Gaussian

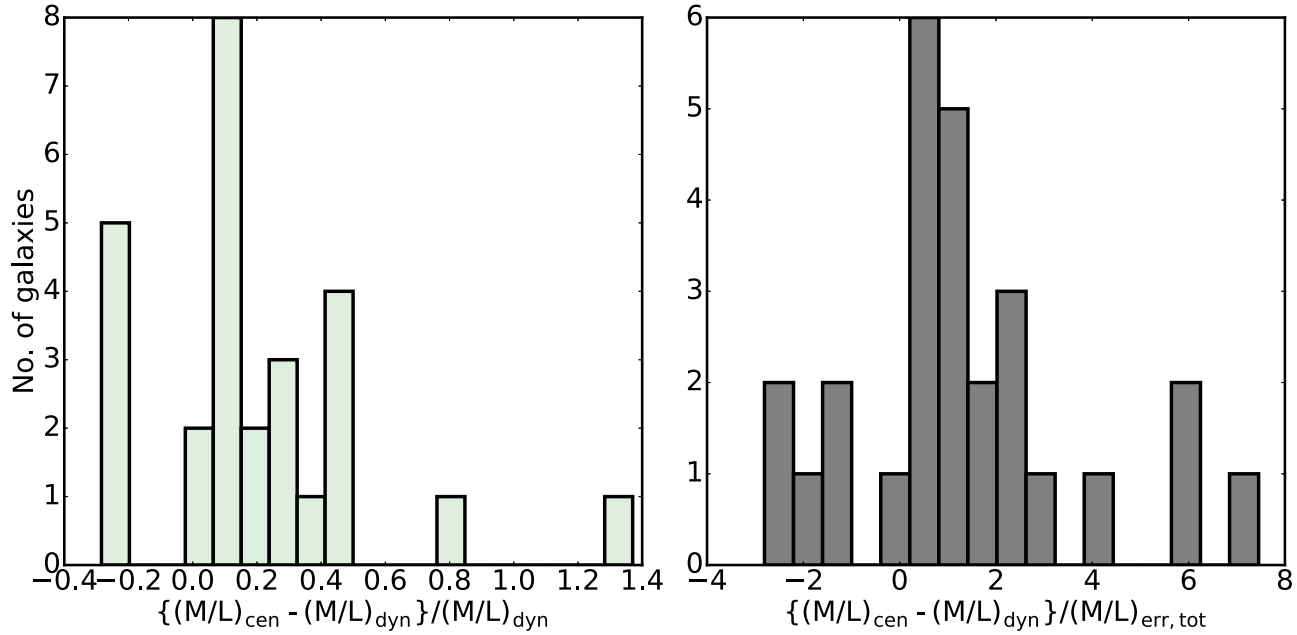

Figure 9. Left panel: distribution of enhancement of central $(M/L)_{\rm cen}$ with respect to $(M/L)_{\rm dyn}$. This indicates the percentage by which $(M/L)_{\rm cen}$ is higher than $(M/L)_{\rm dyn}$; the median enhancement is 14%. Right panel: distribution of the significance of central $(M/L)_{\rm cen}$ of our sample of galaxies. The plot indicates the significance in the enhancement of central M/L. Four high-significance detections are at the right end.

distribution, we calculate that the probability of randomly having 21 of the 27 $(M/L)_{\rm cen}$ values higher than the $(M/L)_{\rm dyn}$ values is just 0.002; therefore, the enhancement is statistically significant at the $>3\sigma$ level based simply on the asymmetry of the distribution.

The right panel of Figure 9 shows the differences relative to the expected errors, showing that some individual objects have highly significant enhancements in $(M/L)_{\rm cen}$. $(M/L)_{\rm err,tot}$ is the total 1σ error that has several sources of error added in quadrature:

$$(M/L)^2_{\rm err,tot} = (M/L)^2_{\rm err,rms} + (M/L)^2_{\rm err,sys} + (M/L)^2_{\rm err,dyn}, \quad (1)$$

where $(M/L)_{\rm err,rms}$ (2%–15%) is error from the measurements of velocity dispersion and $ML_{\rm err,sys}$ (2.5%) is the systematic error (both described in Section 5.2). The $(M/L)_{\rm err,dyn}$ is the error on $(M/L)_{\rm dyn}$; for this error we take the quoted 6% uncertainty given in Cappellari et al. (2013b). We note that same uncertainty is assumed for both $(M/L)_{\rm err,sys}$ and $(M/L)_{\rm err,dyn}$ in all galaxies.

7. Causes of Inflated *M/L*

An enhancement in the central M/L is clearly seen in our sample of galaxies. We have already excluded several systematic effects that could cause this positive bias in the previous sections. Here we discuss additional possibilities.

We start by considering whether the enhanced M/L could be due to gradients in stellar ages and metallicities. Because $(M/L)_{\rm dyn}$ is derived from kinematics at larger radii, any gradient in stellar populations between those radii and the center could lead to differences in the stellar M/L. But based on the stellar population fits to the ATLAS$^{\rm 3D}$ spectra discussed in Section 4.4 and shown in Figure 5, the central $(M/L)_{\rm pop}$ are on average lower than the outer $(M/L)^{\rm out}_{\rm pop}$. The maximum enhancement in the $(M/L)_{\rm cen}$ in Figure 5 is $\sim$7%, which is much lower than the values in Figure 9, which have a median enhancement of $\sim$14%. Thus, based on stellar population variations alone, we would expect a *decline* in the central M/L for most galaxies, not the increase that is observed. Including these variations in stellar population M/L as a correction to the $(M/L)_{\rm cen}$ comparison to $(M/L)_{\rm dyn}$, we find enhanced $(M/L)_{\rm cen}$ in 21 of 27 galaxies, with a median enhancement of 18%, very similar to the values found without correction. This strongly suggests that a metallicity or stellar age gradient cannot be the reason for an enhancement in the M/L.

These stellar population gradients may provide an explanation for the negative tail of the distribution extending to higher significance than expected based on our error estimates. This could happen if metallicity or stellar age gradients lead to an underestimation of the central $(M/L)_{\rm cen}$. We find that five out of six galaxies with decreased central M/Ls have a younger population at their centers.

Overall, this leaves us with three possible explanations for the enhanced $(M/L)_{\rm cen}$ values:

1. The presence of massive BHs in these galaxies.
2. Radial IMF variations in the galaxy.
3. Variations in anisotropy.

We focus on these three explanations in the next sections. If we assume that the $(M/L)_{\rm cen}$ enhancements are due to the presence of central BHs, we can derive BH masses for these galaxies and compare these to previous dynamical estimates. We also constrain the scatter in the M–σ relationship using the enhancement in the central M/L. Then in the following subsections, we discuss the possibility of radial IMF variations and the effects of anisotropy in determination of M/L.

7.1. Massive Black Holes

The nuclei's elevated M/L may be due to the presence of a BH; if this were the case, we could use these to estimate the BH mass required to account for the apparent change in M/L. This

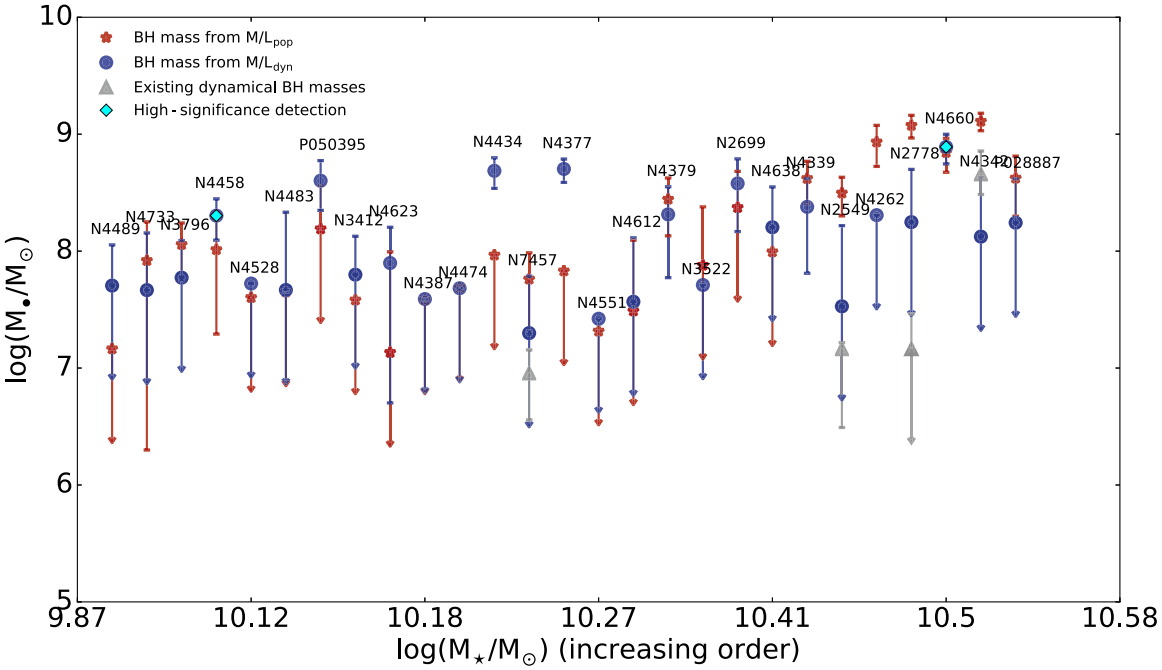

Figure 10. Estimated BH masses and their upper limits for galaxies calculated using JAM models based on the observed enhancement in the $(M/L)_{\rm cen}$. These are plotted from lowest to highest stellar masses. The BH masses calculated using $(M/L)_{\rm dyn}$ are plotted in blue, whereas BH masses calculated using $(M/L)_{\rm pop}$ are plotted in red. Previously known BH masses are plotted in gray. We highlight the two highest-significance detections as cyan diamonds.

approach is essentially identical to that of Mieske et al. (2013), who suggested BHs as the explanation for enhanced M/Ls in UCDs. Estimates of BH masses for each galaxy were derived using JAM models based on the central velocity dispersion and taking $(M/L)_{\rm dyn}$ (calculated outside the nucleus) as the true stellar M/L. The amount by which $(M/L)_{\rm cen}$ is higher than $(M/L)_{\rm dyn}$ therefore directly translates to a best-fit BH mass. We also derived BH masses considering the $(M/L)_{\rm pop}$ values as the true stellar M/L. The errors on our BH mass estimates are directly translated from the errors as described in Section 5.2. We also get the upper limits for the galaxies' BH masses, where $(M/L)_{\rm cen} < (M/L)_{\rm dyn}$, by considering the minimum limit to be $(M/L)_{\rm dyn}$ and adding the 1σ error to it. Figure 10 shows our calculated BH masses based on $(M/L)_{\rm dyn}$ and $(M/L)_{\rm pop}$, ranked in increasing order of their galaxy mass. Using $(M/L)_{\rm dyn}$, we find nine galaxies with $>1\sigma$ enhancements; these galaxies have BH mass estimates ranging from $\sim 8 \times 10^7\ M_\odot$ to $\sim 8 \times 10^8\ M_\odot$. Our upper limits are all above $\sim 10^7\ M_\odot$, suggesting that we do not have a sensitivity to BHs below this mass limit using this technique. The estimated BH masses, M–σ relation predictions, and sizes of the central regions for each galaxy are shown in Table 3.

In Figure 11, we show the same BH mass estimates, but plotted against galaxy velocity dispersion σ_e. The bottom histogram shows that our sample falls below the dispersion of most previous dynamical BH mass estimates. All of our estimated BH masses lie clearly above the M–σ relationship.

We stress that the BH masses inferred here are crude estimates and our upper limits are very dependent on the determination of our errors. Nonetheless, the UCD case shows that the $\sim$10% mass fraction BHs that were suggested by the similar Mieske et al. (2013) analysis have in fact been found using high-resolution spectroscopy (Seth et al. 2014; Ahn et al. 2017), and the sizes of the nuclear M/L enhancements we see in the lower-mass ATLAS^{3D} ETGs are comparable to the level of enhancements we expect if similar BHs exist in these galaxies (see Section 2).

Using the estimated BH masses, we calculate the sphere of influence (SOI) radius, $r_{\rm SOI} = G.M_\bullet/\sigma_e^2$, listed in Table 3. The median $r_{\rm SOI}$ of 38 pc is comparable in size to the median pixel size of our sample galaxies of 75 pc (also listed in Table 3). However, the $r_{\rm SOI}$ is also significantly smaller than the central pixel size in some cases, as expected when the stellar component dominates the kinematics of the central pixel; this does not in principle prevent us from correctly estimating the BH mass. We note that the mass models of our galaxies have a median pixel size (from *HST* imaging) of 4 pc; variations in the mass model on scales smaller than this could lead to systematic errors in our BH mass estimates.

We highlight particularly interesting objects here.

Two galaxies, NGC 4458 and NGC 4660, show $\gtrsim 3\sigma$ enhancements in $(M/L)_{\rm cen}$ relative to both the $(M/L)_{\rm dyn}$ and $(M/L)_{\rm pop}$ values. Both have robust mass models, are not affected by significant central color gradients, and are therefore our strongest candidates for BH detections. In both cases, the BHs inferred are much more massive than the prediction from the M–σ relation (70 times and 6 times, respectively). NGC 4458 is a relatively low mass ETG ($M_\star = 1.07 \times 10^{10}\ M_\odot$), while NGC 4660 is about three times more massive.

Two other objects, NGC 4377 and NGC 4434, also have a $>3\sigma$ enhancement of $(M/L)_{\rm cen}$ relative to $(M/L)_{\rm dyn}$, but are not at all enhanced relative to $(M/L)_{\rm pop}$. This could be due to errors in the low-quality Cappellari et al. (2013a) dynamical models (quality values of 0 and 1, respectively), and we do not consider either of these as robust BH candidates. An additional nine objects, mostly at the high-mass end, have $>3\sigma$ enhancements in $(M/L)_{\rm pop}$ but $<3\sigma$ enhancements in $(M/L)_{\rm dyn}$; of these, NGC 4339 and NGC 4379 have the most

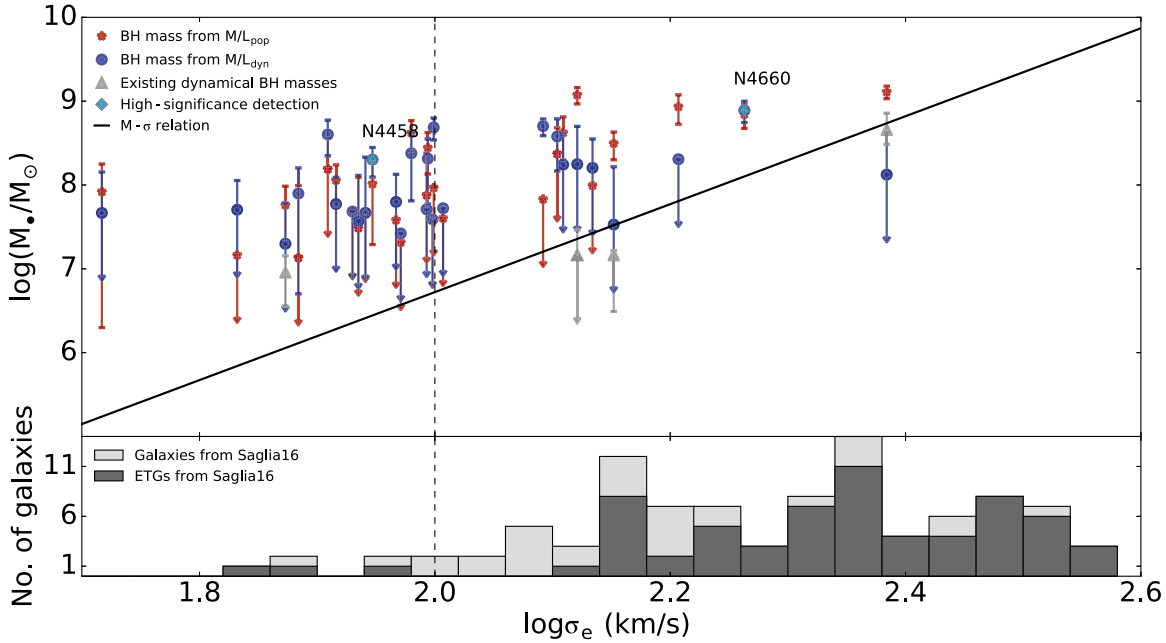

Figure 11. Top panel: estimated BH masses plotted in conjunction with the $M_\bullet$–σ relationship (solid line). Our method is sensitive only to BHs with masses higher than expected from the $M_\bullet$–σ relationship. Symbols as in Figure 10. Bottom panel: distribution of velocity dispersion of galaxies from Saglia et al. (2016). Note that there are very few ETGs having $\sigma < 100$ km s^{-1} and we are probing this low velocity dispersion region.

significant $(M/L)_{\rm dyn}$ enhancements and are most likely to be BH detections. However, for the bulk of these objects, we suspect that they have an IMF heavier than the Kroupa IMF, as suggested by their high $(M/L)_{\rm dyn}$ values at larger radii (Cappellari et al. 2012, 2013a). To recap, we have enhancement in central M/L, $>1\sigma$ for 14 galaxies, $>2\sigma$ for 8 galaxies, and $>3\sigma$ for 4 galaxies with respect to $(M/L)_{\rm dyn}$.

7.1.1. Comparing BH Masses with Existing BH Masses

Five galaxies in our sample have existing dynamical measurements of BH masses or upper limits (as compiled by Kormendy & Ho 2013). These are also plotted in Figure 10 (in gray): NGC 2549, NGC 2778, NGC 3377, NGC 4342, and NGC 7457. Note that the existing measurement in NGC 2549 is a weak detection (Krajnović et al. 2009) and NGC 2778 only has a BH mass upper limit (Schulze & Gebhardt 2011).

For NGC 3377 (not shown owing to its color gradient), we get an $(M/L)_{\rm cen}$ of 4.09, which, compared to the $(M/L)_{\rm dyn}$ of 3.57, suggests an $M_{\rm BH} = 9 \times 10^7\ M_\odot$, which is consistent with its existing BH mass. In the other four galaxies, all the BH mass estimates are consistent with our BH upper limits determined from $(M/L)_{\rm dyn}$. However, many of them have much higher inferred BH masses from $(M/L)_{\rm pop}$; we take this as further evidence that our enhancements in $(M/L)_{\rm cen}$ relative to $(M/L)_{\rm pop}$ values are not due to BHs, at least for galaxies above $\sim 10^{10.4}\ M_\odot$. Instead, these enhancements in dynamical versus population M/Ls in both the center and outer regions suggest global IMF variations. As noted in the Introduction, the sample of existing BH masses in this mass range of ETGs is minimal, and none of our strongest BH candidates have previously published dynamical BH mass estimates. However, there are existing central X-ray measurements for NGC 4660 (4.46×10^{38} erg s^{-1}), NGC 4379 (4.16×10^{38} erg s^{-1}), and NGC 4458 ($<2.13 \times 10^{38}$ erg s^{-1}) (Gallo et al. 2010).

To further check the accuracy of our measured BH masses, we considered a sample of 10 high-mass ETGs ($\log(M_*/M_\odot) > 10.5$) from the ATLAS^{3D} sample that had existing dynamical BH mass estimates from Saglia et al. (2016). We modeled those galaxies in a similar way using JAM models, as we did earlier, and estimated the BH masses. Eight out of 10 of these galaxies had BH masses within the 1σ range of their existing BH measurements.

7.1.2. Constraining the Scatter in $M_\bullet$–σ Relationship

We now describe how we can use our existing measurements of the enhancement of $(M/L)_{\rm cen}$ to $(M/L)_{\rm dyn}$ to constrain the scatter in the $M_\bullet$–σ relationship. A large scatter in this mass range of galaxies would result in some of our galaxies having unusually massive BHs that would be detectable as enhancements in $(M/L)_{\rm cen}$.

We first start by predicting the BH masses in each galaxy assuming the $M_\bullet$–σ relationship from Saglia et al. (2016):

$$\log M_\bullet = 5.246 \times \log \sigma_e - 3.77. \quad (2)$$

The σ_e used here is the effective stellar velocity dispersion adopted from Table 1 (Cappellari et al. 2013b). They were calculated by co-adding all SAURON spectra within an effective ellipse of area πR_e^2, where R_e is the effective radius. The expected $M_\bullet$ over the range of σ_e values of our galaxies are shown as a line in Figure 11 and are given for each galaxy in Table 3. Our BH mass estimates are not sensitive to any BHs that fall on the $M_\bullet$–σ relationship; thus, we will only detect BHs when they are significantly more massive than expected. We can therefore constrain the scatter in the $M_\bullet$–σ relationship through our most significant detections.

Simulations are performed to predict the central M/L of the galaxies from the $M_\bullet$–σ relationship with scatter. Specifically, we use the $M_\bullet$–σ relationship from Equation (2) and add

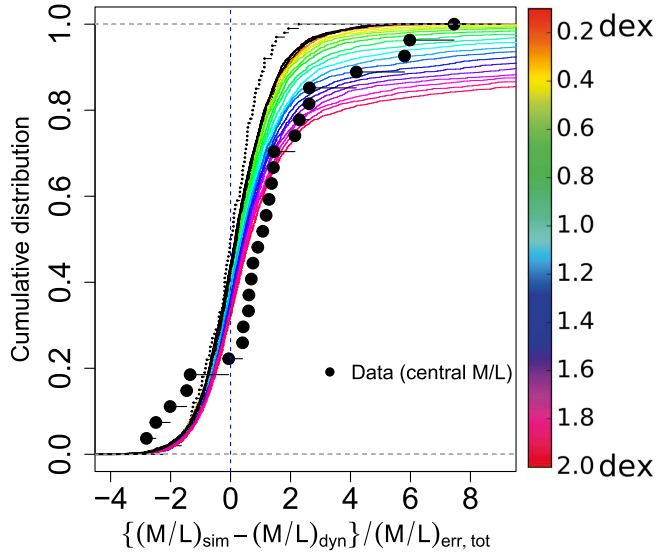

Figure 12. Results from our simulations to constrain the scatter in the $M_\bullet$–σ relationship. Comparison of the ECDFs of the enhancement in central M/L between simulations and data. The filled points are the ECDFs of the original data (right panel of Figure 9). The dashed black line shows a simulation with no BH including only the errors and is therefore a Gaussian distribution; the solid black line shows the effect of adding $M_\bullet$–σ relationship BHs to each galaxy in our sample. Colored lines show simulations with a range of scatter in the $M_\bullet$–σ relationship. The scatter increases from top to bottom, ranging from 0.1 to 2.0 dex.

random scatter to it ranging from 0.0 to 2.0 dex. A BH mass is computed based on the σ_e of the galaxy, with the scatter added in as a Gaussian random variable. Using our luminosity models for each galaxy, we predict the central velocity dispersion by assuming that the central M/L of the galaxies is equal to $(M/L)_{\rm dyn}$ and adding the effect of the BH. Then, we simulate our observations by adding a 1σ Gaussian random error based on the observed dispersion error from ATLAS$^{\rm 3D}$. We then derive an M/L from this dispersion using a JAM model, just as we have for our observed data; we add a 2.5% Gaussian error to account for the systematic effects of the luminosity models, which yields our final $(M/L)_{\rm sim}$ value. The $(M/L)_{\rm sim}$ value is then compared to the $(M/L)_{\rm dyn}$ to determine the enhancement relative to the error. For each level of scatter in the M–σ relationship, we run 1000 simulations per galaxy and calculate the $\{(M/L)_{\rm sim} - (M/L)_{\rm dyn}\}/(M/L)_{\rm err,tot}$ for the full set of galaxies. Empirical cumulative distribution functions (ECDFs) of these simulations are shown as the colored lines in Figure 12 and can be compared to the ECDF of the observed data (filled points), which is the cumulative version of the right panel of Figure 9.

The difference between the dashed black line (the no-BH model, including only measurement errors) and the solid black line (a model with $M_\bullet$–σ relation BHs with no scatter) shows that despite being far below our mass sensitivity for individual detections, the presence of $M_\bullet$–σ BHs does have a clear effect on the expected ECDFs, increasing the number of enhanced M/L objects we would expect.

Two trends are apparent comparing the observed and model ECDFs. First, the central M/L enhancement of 0 to 2σ does not seem to be consistent with being caused by $M_\bullet$–σ relation BHs regardless of the scatter. We think that the most likely cause of these enhanced central M/Ls are radial IMF variations, which we discuss further in the next subsection. Second, the models with $M_\bullet$–σ scatter above $\sim$1 dex would clearly result in detections of more enhanced $(M/L)_{\rm cen}$ values than we observe. Our highest outlier $(M/L)_{\rm cen}$ is enhanced by 7.5σ relative to $(M/L)_{\rm dyn}$, and we can use this maximum value to put a limit on the scatter in the $M_\bullet$–σ relation for $\sim 10^{10}\ M_\odot$ ETGs.

To quantify these constraints, we examine our 1000 simulations and see how often a single simulation would give an $(M/L)_{\rm cen}$ enhancement larger than the highest outlier in our data. We find that when the scatter is sufficiently large (>1.2 dex), 95% of our simulations predict a central M/L greater than 7.5σ. On the other hand, when it is below 0.4 dex, only 5% of the simulations predict it. Thus, with 95% confidence, we can constrain that the scatter in the $M_\bullet$–σ relation for our low-mass ETGs is between 0.4 and 1.2 dex. Recent measurements suggest a scatter in the $M_\bullet$–σ relation of $\sim$0.4 dex for the mostly higher dispersion galaxies with existing dynamical BH mass measurements (e.g., Greene et al. 2016; Saglia et al. 2016), suggesting that the scatter either stays constant or grows in these lower-mass ETGs.

7.2. Radial IMF Variations in the Galaxies

Apart from BHs, another plausible cause for the increase in $(M/L)_{\rm cen}$ relative to $(M/L)_{\rm dyn}$ are radial gradients in the IMF. Evidence for enhancements in the number of low-mass stars has been suggested both from spectroscopic studies of dwarf-sensitive lines (e.g., van Dokkum & Conroy 2010, 2011; Conroy & van Dokkum 2012; Spiniello et al. 2012; La Barbera et al. 2017) and dynamically owing to higher measured M/Ls (e.g., Cappellari et al. 2012; Tortora et al. 2013; Lyubenova et al. 2016). Recent work has explored whether these IMF variations are radially varying within the galaxies, with a mix of results, including some evidence for increasingly strong dwarf-sensitive line indices in the central regions of galaxies ($\sim$300 pc; Spiniello et al. 2014; Martín-Navarro et al. 2015; McConnell et al. 2016). For example, Martín-Navarro et al. (2015) find that the IMF slope varies from $\alpha = 3.0$ at the center to $\sim$1.8 at an effective radius, with most of the change being within $0.2R_e$. However, the recent work of Davis & McDermid (2017) shows a wide range of behavior in the apparent radial IMF gradients.

The largest variations in IMF appear to occur in the most massive, highest-dispersion galaxies, and therefore most studies on global and radial IMF variations have focused on galaxies with $\sigma > 200\ {\rm km\ s^{-1}}$. However, our sample is quite different from most of the galaxies in these previous studies of the IMF, with all but one of our galaxies having $\sigma < 200\ {\rm km\ s^{-1}}$.

We have shown above that the small enhancements in $(M/L)_{\rm cen}$ relative to the $(M/L)_{\rm dyn}$ derived at larger radii are seen in a majority of our galaxies. These enhancements are not easily interpreted as being due to BHs drawn from the $M_\bullet$–σ relation; our measured ECDF in Figure 12 has many more galaxies at +0–2σ enhancements than any of the BH models. The typical $(M/L)_{\rm cen}$ enhancements in our galaxies are $\sim$14% (Figure 9), and the M/L variation expected from the inferred IMF variations in massive galaxies can be significantly larger than this (Davis & McDermid 2017). Thus, it is plausible that small changes in the IMF slope could be creating the enhanced M/L we observe.

We tested the amount of change in the IMF slope that would be required to generate an enhancement of 14% in the inferred M/L. We find that a small change in the IMF slope from $\alpha = 2.3$ to $\sim$2.4 is enough to create this difference. We also

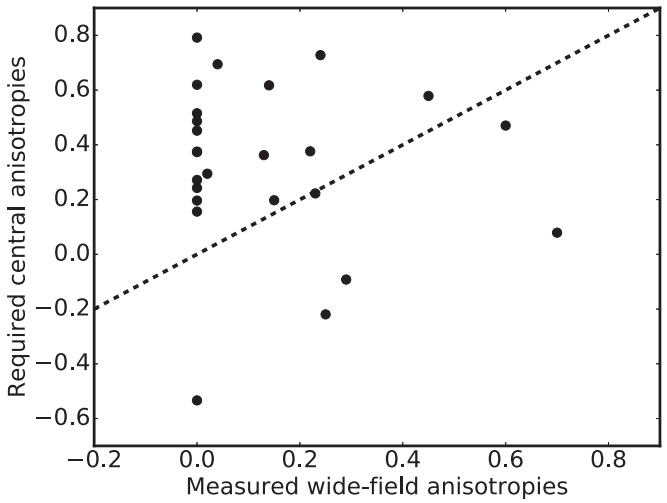

Figure 13. Comparison of the anisotropies derived from model fits within $1R_e$ (x-axis; Cappellari et al. 2013b), with the required anisotropies to eliminate the enhancement in the $(M/L)_{\rm cen}$ (y-axis). The distribution of anisotropies at larger radii has a median of just 0.09, while much higher values would be required to explain the enhancement in central M/L.

derived the inferred M/L for the galaxies from the BH masses calculated from the M–σ relationship. The inclusion of these BHs only slightly lowers the median M/L enhancement to 12%. We also note that the stellar population variations shown in Figure 5 would make this M/L enhancement larger. In any of these cases, a small change in the IMF slope could be responsible for the M/L enhancements, with the IMF being steeper in the center compared to their outer regions.

7.3. Impact of Anisotropy

Differences from the anisotropies assumed in our models may also lead to variations in central M/L. Since we model only the central pixel, it is not possible to fit for the anisotropy. Therefore, we assume that the anisotropy remains constant, and that it is the same in the center as the best-fit value from the full FOV (Cappellari et al. 2013b).[12] This assumption is not necessarily true, as anisotropy can vary with radius (e.g., Gebhardt et al. 2011; Yıldırım et al. 2015).

To test whether the variation in anisotropies could possibly explain the enhancement in $(M/L)_{\rm cen}$ relative to $(M/L)_{\rm dyn}$, we calculate the anisotropy that is required to eliminate this enhancement. Specifically, we create JAM models over a range of anisotropies and find where the best-fit $(M/L)_{\rm cen}$ matches the $(M/L)_{\rm dyn}$, thus undoing the enhancement in the central M/L. We then compare the anisotropies required to eliminate this enhancement in each galaxy against the distribution of anisotropies inferred at larger radii.

Figure 13 shows the comparison between these two anisotropy values. The median of the anisotropies at large radii was found to be 0.09 for our sample of galaxies. We also calculated the median of anisotropies for the whole sample of 260 ATLAS^{3D} galaxies, which was found to be 0.05. Significantly higher radial anisotropy at the centers of these galaxies (median $\sim$ 0.6) would be required to explain the enhanced $(M/L)_{\rm cen}$ values. We think that this large of an enhancement in anisotropy at the centers of a majority of our galaxies is unlikely.

[12] Available from http://purl.org/atlas3d.

8. Summary and Discussion

In this work, we have examined the central dynamical M/Ls of a sample of 27 low-mass ($<3\times10^{10}\,M_\odot$) early-type galaxies. For each galaxy, we construct a high-resolution luminosity/mass model from *HST* data. We combine this with the central velocity dispersion data from ATLAS^{3D} to infer the central $(M/L)_{\rm cen}$ using JAM modeling. We exclude galaxies with dust features and strong color gradients that would affect the reliability of our modeling, which assumes that mass traces light. We then compare our central $(M/L)_{\rm cen}$ values to expectations from stellar population models ($(M/L)_{\rm pop}$) and dynamical measurements at larger radii made by the ATLAS^{3D} team ($(M/L)_{\rm dyn}$; Cappellari et al. 2013a).

The results of our study are as follows:

1. The $(M/L)_{\rm cen}$ is elevated for $\sim$80% of galaxies in the sample as compared to both $(M/L)_{\rm dyn}$ and $(M/L)_{\rm pop}$. This enhancement is statistically significant (3.3σ) over the full sample of galaxies, although many individual galaxies have only small enhancements.
2. We examine systematic and random errors in our measurements and find that they cannot explain the enhancement we see. The elevation in the $(M/L)_{\rm cen}$ can be best described by a combination of central BHs or radial IMF variations within these galaxies.
3. Two galaxies, NGC 4458 and NGC 4660, have $\gtrsim3\sigma$ enhancements in $(M/L)_{\rm cen}$ relative to both $(M/L)_{\rm dyn}$ and $(M/L)_{\rm pop}$. We suggest that these are due to BHs with a mass of $\sim2\times10^8\,M_\odot$ in NGC 4458 and $\sim8\times10^8\,M_\odot$ in NGC 4660.
4. Based on the comparison of $(M/L)_{\rm cen}$ to $(M/L)_{\rm dyn}$ and $(M/L)_{\rm pop}$, we estimate the BH masses (and upper limits) for each galaxy; in general, these are upper limits above the expected values for the $M_\bullet$–σ relationship.
5. We use the enhancements in $(M/L)_{\rm cen}$ relative to $(M/L)_{\rm dyn}$ to estimate a minimum and maximum scatter on the $M_\bullet$–σ relationship of 0.4 and 1.2 dex at 95% confidence. The upper limit is a firm one, as models with larger scatter would produce even more significant enhancements in $(M/L)_{\rm cen}$ than we observe.
6. The distribution of $(M/L)_{\rm cen}$ enhancements is not well explained just by BHs; therefore, we consider the possibility that they are due to radial IMF variations. Small variations in the IMF can account for the typical $\sim$14% enhancement seen in the $(M/L)_{\rm cen}$ values relative to the $(M/L)_{\rm dyn}$ calculated at larger radii.

We now return to the discussion in Section 2 on whether low-mass ETGs can act as the progenitors for UCDs. Putting the BHs observed at the centers of UCDs (Seth et al. 2014; Ahn et al. 2017) into typical ETGs reduces the enhancement in velocity dispersion and inferred M/L. Nonetheless, in our simulation adding a galaxy around M60-UCD1, we find an expected enhancement of $\sim$12% in the M/L due to the presence of a BH. This enhancement is very comparable to the median enhancement of $\sim$14% that we see in our sample of low-mass ETGs. This supports the fact that UCDs can in fact be considered as nuclear remnants of ETGs.

Very few BHs are known in ETGs with masses $\lesssim10^{10}\,M_\odot$ and $\sigma\lesssim100$ km s^{-1}. We have shown that deriving the central

M/L for nearby low-mass ETGs from ground-based spectroscopy can be a good probe for finding possible BHs. While in individual galaxies we are sensitive only to BHs significantly more massive than expected from the $M_\bullet$–σ relation, the overall distribution of central M/L is sensitive to the scatter in this relation. We plan to follow up this work with adaptive optics observations of some of the most promising massive BH candidates, as well as examination of these galaxies at X-ray and radio wavelengths (e.g., Gallo et al. 2010). We also find some evidence for radial IMF variations; more conclusive evidence could be gained from spectroscopic observations of IMF-sensitive features across these galaxies.

R.P. and A.S. acknowledge support for this work from *HST* AR-14313. A.S. is also supported by NSF AST-1350389. J.S. acknowledges support from NSF grant AST-1514763 and the Packard Foundation. We thank Frank van den Bosch for his help with data on NGC 4342. Based on observations made with the NASA/ESA *Hubble Space Telescope* and obtained from the Hubble Legacy Archive, which is a collaboration between the Space Telescope Science Institute (STScI/NASA), the Space Telescope European Coordinating Facility (ST-ECF/ESA), and the Canadian Astronomy Data Centre (CADC/NRC/CSA).

Appendix
List of Parameters for the Sample of Galaxies

We present here Table 2 and Table 3 which contain the list of All 27 galaxies from our sample. Table 2 contains the central *M/L*s that were derived using the central velocity dispersion values and the mass models for each galaxy. It also shows the filters in which the mass models were obtained. There are also

Table 2
Mass-to-light Ratios, Central Velocity Dispersions, and *HST* Imaging Data of All 27 Galaxies

Galaxy	$(M/L)_{\rm cen}$(Low–High) $(M_\odot/L_\odot)$	$(M/L)_{\rm dyn}$ $(M_\odot/L_\odot)$	Quality for $(M/L)_{\rm dyn}$	$(M/L)_{\rm pop}$ $(M_\odot/L_\odot)$	$\sigma_\circ$ (km s^{-1})	Camera	Filter (for Models)	Filters (for Colors)
(1)	(2)	(3)	(4)	(5)	(6)	(7)	(8)	(9)
NGC 2549	4.80 (4.51–5.11)	4.66	3	3.42	149.80 ± 2.79	WFPC2/PC	F702W	···
NGC 2699	4.48 (4.06–4.91)	3.46	1	3.84	151.67 ± 5.30	WFPC2/PC	F702W	···
NGC 2778	7.42 (6.98–7.87)	6.95	2	4.23	183.63 ± 3.22	WFPC2/PC	F814W	F814W, F555W
NGC 3412	1.87 (1.71–2.04)	1.64	1	2.38	103.94 ± 3.34	WFPC2/PC	F606W	···
NGC 3522	3.07 (2.54–3.64)	3.86	0	2.73	101.76 ± 7.89	WFC3/UVIS	F814W	F814W, F475W
NGC 3796	2.15 (1.87–2.44)	1.78	0	1.43	94.35 ± 5.07	WFPC2/WF3	F814W	F814W, F606W
NGC 4262	5.60 (5.30–5.90)	5.63	2	4.17	207.69 ± 2.96	ACS/WFC	F475W	···
NGC 4339	6.09 (5.46–6.74)	4.83	0	3.87	138.57 ± 5.57	WFPC2/PC	F606W	···
NGC 4342	11.14 (10.2–12.1)	10.43	3	4.23	317.10 ± 10.60[a]	WFPC2/PC	F814W	F814W, F555W
NGC 4377	3.63 (3.37–3.89)	1.97	0	3.75	152.34 ± 3.48	WFPC2/PC	F606W	F850LP, F475W
NGC 4379	4.90 (4.49–5.33)	3.99	1	3.67	130.97 ± 3.97	WFPC2/PC	F814W	F814W, F555W
NGC 4387	2.84 (2.50–3.19)	3.75	1	3.68	92.90 ± 4.51	ACS/WFC	F475W	F850LP, F475W
NGC 4434	3.86 (3.65–4.08)	2.61	1	4.00	140.69 ± 2.09	ACS/WFC	F475W	F850LP, F475W
NGC 4458	4.30 (3.92–4.68)	2.88	1	3.57	120.69 ± 3.80	WFPC2/PC	F814W	F814W, F555W
NGC 4474	2.42 (1.97–2.90)	3.03	2	3.07	88.08 ± 7.37	WFPC2/PC	F702W	F850LP, F475W
NGC 4483	3.22 (2.66–3.82)	3.01	1	3.45	88.27 ± 6.86	ACS/WFC	F475W	F850LP, F475W
NGC 4489	1.34 (0.99–1.72)	0.98	0	1.74	55.49 ± 6.85	ACS/WFC	F475W	F850LP, F475W
NGC 4528	2.85 (2.54–3.16)	3.80	2	2.88	112.12 ± 4.68	ACS/WFC	F475W	F850LP, F475W
NGC 4551	3.56 (2.87–4.31)	4.98	2	3.89	97.33 ± 8.59	ACS/WFC	F475W	F850LP, F475W
NGC 4612	1.63 (1.39–1.87)	1.50	0	1.52	82.91 ± 5.01	WFPC2/PC	F606W	F850LP, F475W
NGC 4623	3.02 (2.28–3.85)	2.10	1	2.86	61.15 ± 7.15	ACS/WFC	F475W	F850LP, F475W
NGC 4638	3.06 (2.80–3.33)	2.71	3	3.65	132.29 ± 4.06	ACS/WFC	F475W	F850LP, F475W
NGC 4660	5.96 (5.64–6.27)	4.00	2	4.19	232.18 ± 3.24	WFPC2/PC	F814W	F814W, F555W
NGC 4733	2.79 (1.81–3.94)	2.18	0	1.69	49.85 ± 8.86	WFPC2/PC	F814W	F814W, F555W
NGC 7457	2.03 (1.67–2.42)	1.80	1	1.34	65.11 ± 5.16	WFPC2/PC	F814W	F814W, F555W
PGC 028887	5.05 (4.57–5.53)	4.50	0	3.72	135.84 ± 4.78	WFC3/UVIS	F814W	F814W, F475W
PGC 050395	2.46 (1.89–3.09)	1.04	0	1.91	77.42 ± 8.40	WFC3/UVIS	F814W	F814W, F475W

Notes. Column (1): galaxy's name from LEDA (Paturel et al. 2003), which is used as a standard here. Column (2): central *M/L* derived using JAM models. All the values are in SDSS *r* band. The Low and High values include the errors from velocity dispersions and 2.5% systematic error. Column (3): dynamical M/L derived by dynamically fitting the outer regions of the galaxy (>2″, within $1R_e$); we assume an error of 6% on all of these M/L as given in Cappellari et al. (2013a). Column (4): qual = 0 indicates a low-quality JAM fit that is due to barred galaxies, dust, or uncertain deprojection due to a low inclination of the galaxy; qual = 3 indicates a good JAM fit to the data. Column (5): stellar population M/L derived by fitting the ATLAS^{3D} central spectrum of a galaxy assuming a Kroupa IMF. We assume an error of 6% on all of these M/L as given in Cappellari et al. (2013a). Column (6): central velocity dispersions derived from ATLAS^{3D} kinematic data. Columns (7) and (8): images of galaxies from the *HST* camera and their corresponding filters used in deriving the mass models. Column (9): filters that were used in determining the color maps of the galaxies.

[a] This central velocity dispersion value is taken from van den Bosch et al. (1998).

(This table is available in machine-readable form.)

Table 3
Black Hole Masses, Sphere of Influence, and ATLAS^{3D} and *HST* Pixel Sizes of All 27 Galaxies

Galaxy	σ_e (km s^{-1})	log$M_\star$ ($M_\odot$)	$M_{\bullet,\rm dyn}$(Low–High) ($M_\odot$)	$M_{\bullet,\rm pop}$(Low–High) ($M_\odot$)	$(M-\sigma)_\bullet$ ($M_\odot$)	$r_{\rm SOI}$ (pc)	Pixel Size ATLAS^{3D}(pc)	Pixel Size *HST* (pc)
(1)	(2)	(3)	(4)	(5)	(6)	(7)	(8)	(9)
NGC 2549	2.152	10.435	3.37 (0.00–16.5) × 10^7	3.14 (2.00–4.28) × 10^8	3.31 × 10^7	7.26	56.05	2.98
NGC 2699	2.104	10.387	3.79 (1.47–6.15) × 10^8	2.36 (0.00–4.81) × 10^8	1.85 × 10^7	101.68	119.40	6.35
NGC 2778	2.121	10.497	1.77 (0.00–5.00) × 10^8	1.19 (0.93–1.45) × 10^9	2.27 × 10^7	43.97	101.63	5.41
NGC 3412	1.967	10.162	6.29 (0.00–13.4) × 10^7	0.00 (0.00–3.82) × 10^7	3.54 × 10^6	31.72	50.13	2.67
NGC 3522	1.993	10.305	0.00 (0.00–5.13) × 10^7	7.57 (0.00–23.9) × 10^7	4.84 × 10^6	22.94	116.21	4.95
NGC 3796	1.916	9.987	5.93 (0.00–12.3) × 10^7	1.14 (0.56–1.74) × 10^8	1.91 × 10^6	37.84	103.45	11.01
NGC 4262	2.207	10.479	0.00 (0.00–2.03) × 10^8	8.59 (5.30–11.9) × 10^8	6.43 × 10^7	33.89	70.18	3.73
NGC 4339	1.98	10.433	2.39 (0.65–4.17) × 10^8	4.18 (2.55–5.86) × 10^8	4.14 × 10^6	113.41	72.92	3.88
NGC 4342	2.384	10.521	1.33 (0.00–4.28) × 10^8	1.29 (1.07–1.51) × 10^9	5.45 × 10^8	9.84	75.19	4.00
NGC 4377	2.092	10.246	5.04 (3.87–6.13) × 10^8	0.00 (0.00–6.77) × 10^7	1.60 × 10^7	142.85	81.12	4.31
NGC 4379	1.994	10.269	2.06 (0.59–3.55) × 10^8	2.78 (1.35–4.22) × 10^8	4.90 × 10^6	91.78	72.00	3.83
NGC 4387	1.998	10.182	0.00 (0.00–3.89) × 10^7	0.00 (0.00–3.82) × 10^7	5.15 × 10^6	16.99	81.57	4.34
NGC 4434	1.999	10.21	4.86 (3.44–6.29) × 10^8	0.00 (0.00–9.27) × 10^7	5.21 × 10^6	211.39	102.08	5.43
NGC 4458	1.947	10.032	2.01 (1.24–2.80) × 10^8	1.03 (0.20–1.87) × 10^8	2.78 × 10^6	111.30	74.74	3.98
NGC 4474	1.93	10.187	0.00 (0.00–4.82) × 10^7	0.00 (0.00–4.88) × 10^7	2.26 × 10^6	28.82	71.09	3.78
NGC 4483	1.941	10.138	4.65 (0.00–21.5) × 10^7	0.00 (0.00–4.47) × 10^7	2.59 × 10^6	26.42	76.11	4.05
NGC 4489	1.832	9.866	5.07 (0.00–11.3) × 10^7	0.00 (0.00–1.46) × 10^7	6.93 × 10^5	47.58	70.18	3.73
NGC 4528	2.007	10.123	0.00 (0.00–5.28) × 10^7	0.00 (0.00–4.01) × 10^7	5.74 × 10^6	22.13	72.00	3.83
NGC 4551	1.971	10.262	0.00 (0.00–2.64) × 10^7	0.00 (0.00–2.07) × 10^7	3.71 × 10^6	13.06	73.37	3.90
NGC 4612	1.935	10.265	3.69 (0.00–13.0) × 10^7	3.08 (0.00–12.4) × 10^7	2.40 × 10^6	21.54	75.65	4.02
NGC 4623	1.884	10.17	7.91 (0.50–16.0) × 10^7	1.36 (0.00–9.86) × 10^7	1.30 × 10^6	58.43	79.30	4.22
NGC 4638	2.134	10.408	1.60 (0.00–3.54) × 10^8	0.00 (0.00–9.87) × 10^7	2.66 × 10^7	37.40	79.75	4.24
NGC 4660	2.263	10.499	7.78 (5.57–9.98) × 10^8	6.98 (4.72–9.22) × 10^8	1.26 × 10^8	100.32	68.36	3.64
NGC 4733	1.717	9.877	4.64 (0.00–14.3) × 10^7	8.32 (0.20–17.8) × 10^7	1.73 × 10^5	73.90	66.08	3.51
NGC 7457	1.873	10.218	1.99 (0.00–6.11) × 10^7	5.77 (2.08–9.67) × 10^7	1.14 × 10^6	15.44	58.79	3.13
PGC 028887	2.109	10.534	1.75 (0.00–4.16) × 10^8	4.21 (1.99–6.49) × 10^8	1.97 × 10^7	45.84	186.85	7.95
PGC 050395	1.909	10.145	4.00 (2.23–5.94) × 10^8	1.55 (0.00–3.63) × 10^8	1.76 × 10^6	263.61	169.53	7.21

Note. Column (1): galaxy's name from LEDA (Paturel et al. 2003), which is used as a standard here. Column (2): effective stellar velocity dispersion adopted from Cappellari et al. (2013b). They were calculated by co-adding all SAURON spectra within an effective ellipse of area πR_e^2, where R_e is the effective radius. Column (3): galaxy mass as taken from Cappellari et al. (2013b). Column (4): best-fit BH masses derived using $(M/L)_{\rm dyn}$ as the true stellar M/L in our JAM models. Column (5): best-fit BH masses derived using $(M/L)_{\rm pop}$ as the true stellar M/L in our JAM models. Column (6): expected BH masses from the $M_\bullet$–σ relationship from Equation (2). Galaxies NGC 4458 and NGC 4660 are highly significant detections. Column (7): sphere of influence calculated from the derived BH masses (column (4)) using $r_{\rm SOI} = G.M_\bullet/\sigma_e^2$. Column (8): pixel size of ATLAS^{3D} kinematic data for our sample of galaxies that were derived using the distances from Cappellari et al. (2011). Column (9): pixel size of *HST* images for our sample of galaxies that were derived using the distances from Cappellari et al. (2011).

(This table is available in machine-readable form.)

the filters that were used for deriving the color maps. Table 3 contains the BH masses that were derived using the $M/L_{\rm dyn}$ and $M/L_{\rm pop}$ as the true stellar M/L. It also describes the expected sphere of influence based on our derived BH masses and the comparison between the pixel size of the ATLAS^{3D} data and the HST data.

ORCID iDs

Michele Cappellari https://orcid.org/0000-0002-1283-8420
Jay Strader https://orcid.org/0000-0002-1468-9668

References

Ahn, C. P., Seth, A. C., den Brok, M., et al. 2017, ApJ, 839, 72
Bacon, R., Copin, Y., Monnet, G., et al. 2001, MNRAS, 326, 23
Bendinelli, O. 1991, ApJ, 366, 599
Bressan, A., Marigo, P., Girardi, L., et al. 2012, MNRAS, 427, 127
Bruzual, G., & Charlot, S. 2003, MNRAS, 344, 1000
Cappellari, M. 2002, MNRAS, 333, 400
Cappellari, M. 2008, MNRAS, 390, 71
Cappellari, M. 2016, ARA&A, 54, 597
Cappellari, M., Emsellem, E., Krajnović, D., et al. 2011, MNRAS, 413, 813
Cappellari, M., McDermid, R. M., Alatalo, K., et al. 2012, Natur, 484, 485
Cappellari, M., McDermid, R. M., Alatalo, K., et al. 2013a, MNRAS, 432, 1862
Cappellari, M., Scott, N., Alatalo, K., et al. 2013b, MNRAS, 432, 1709
Conroy, C., & van Dokkum, P. 2012, ApJ, 747, 69
Dabringhausen, J., Fellhauer, M., & Kroupa, P. 2010, MNRAS, 403, 1054
Dabringhausen, J., Kroupa, P., & Baumgardt, H. 2009, MNRAS, 394, 1529
Davis, T. A., & McDermid, R. M. 2017, MNRAS, 464, 453
Emsellem, E., Monnet, G., & Bacon, R. 1994, A&A, 285, 723
Frank, M. J., Hilker, M., Mieske, S., et al. 2011, MNRAS, 414, L70
Gallo, E., Treu, T., Marshall, P. J., et al. 2010, ApJ, 714, 25
Gebhardt, K., Adams, J., Richstone, D., et al. 2011, ApJ, 729, 119
Gebhardt, K., Bender, R., Bower, G., et al. 2000, ApJL, 539, L13
Goddard, D., Thomas, D., Maraston, C., et al. 2017, MNRAS, 466, 4731
Graham, A. W., & Scott, N. 2015, ApJ, 798, 54
Greene, J. E., Seth, A., Kim, M., et al. 2016, ApJL, 826, L32
Hąsegan, M., Jordán, A., Côté, P., et al. 2005, ApJ, 627, 203
Kormendy, J., Fisher, D. B., Cornell, M. E., & Bender, R. 2009, ApJS, 182, 216
Kormendy, J., & Ho, L. C. 2013, ARA&A, 51, 511
Krajnović, D., McDermid, R. M., Cappellari, M., & Davies, R. L. 2009, MNRAS, 399, 1839
Krist, J. E., Hook, R. N., & Stoehr, F. 2011, Proc. SPIE, 8127, 81270J
Kroupa, P. 2001, MNRAS, 322, 231
La Barbera, F., Vazdekis, A., Ferreras, I., et al. 2017, MNRAS, 464, 3597
Läsker, R., Greene, J. E., Seth, A., et al. 2016, ApJ, 825, 3
Li, H., Ge, J., Mao, S., et al. 2017, ApJ, 838, 77

Lyubenova, M., Martín-Navarro, I., van de Ven, G., et al. 2016, MNRAS, 463, 3220
Magorrian, J., Tremaine, S., Richstone, D., et al. 1998, AJ, 115, 2285
Martín-Navarro, I., Barbera, F. L., Vazdekis, A., Falcón-Barroso, J., & Ferreras, I. 2015, MNRAS, 447, 1033
McConnell, N. J., Lu, J. R., & Mann, A. W. 2016, ApJ, 821, 39
McConnell, N. J., & Ma, C.-P. 2013, ApJ, 764, 184
McDermid, R. M., Alatalo, K., Blitz, L., et al. 2015, MNRAS, 448, 3484
Mieske, S., Frank, M. J., Baumgardt, H., et al. 2013, A&A, 558, A14
Miller, B., Gallo, E., Treu, T., & Woo, J.-H. 2012, ApJ, 747, 57
Miller, B. P., Gallo, E., Greene, J. E., et al. 2015, ApJ, 799, 98
Nguyen, D. D., Seth, A. C., den Brok, M., et al. 2017, ApJ, 836, 237
Norris, M. A., Kannappan, S. J., Forbes, D. A., et al. 2014, MNRAS, 443, 1151
Paturel, G., Petit, C., Prugniel, P., et al. 2003, A&A, 412, 45
Pfeffer, J., & Baumgardt, H. 2013, MNRAS, 433, 1997
Posacki, S., Cappellari, M., Treu, T., Pellegrini, S., & Ciotti, L. 2015, MNRAS, 446, 493
Rose, J. A., Arimoto, N., Caldwell, N., et al. 2005, AJ, 129, 712
Saglia, R. P., Opitsch, M., Erwin, P., et al. 2016, ApJ, 818, 47
Salpeter, E. E. 1955, ApJ, 121, 161
Savorgnan, G. A. D., Graham, A. W., Marconi, A., & Sani, E. 2016, ApJ, 817, 21
Schulze, A., & Gebhardt, K. 2011, ApJ, 729, 21
Seth, A. C., van den Bosch, R., Mieske, S., et al. 2014, Natur, 513, 398
Spiniello, C., Trager, S., Koopmans, L. V. E., & Conroy, C. 2014, MNRAS, 438, 1483
Spiniello, C., Trager, S. C., Koopmans, L. V. E., & Chen, Y. P. 2012, ApJL, 753, L32
Strader, J., Seth, A. C., Forbes, D. A., et al. 2013, ApJL, 775, L6
Thomas, D., Maraston, C., Bender, R., & Mendes de Oliveira, C. 2005, ApJ, 621, 673
Tortora, C., Romanowsky, A. J., & Napolitano, N. R. 2013, ApJ, 765, 8
van den Bosch, F. C., Jaffe, W., & van der Marel, R. P. 1998, MNRAS, 293, 343
van den Bosch, R. C. E., & de Zeeuw, P. T. 2010, MNRAS, 401, 1770
van Dokkum, P. G., & Conroy, C. 2010, Natur, 468, 940
van Dokkum, P. G., & Conroy, C. 2011, ApJL, 735, L13
Verolme, E. K., Cappellari, M., Copin, Y., et al. 2002, MNRAS, 335, 517
Yıldırım, A., van den Bosch, R. C. E., van de Ven, G., et al. 2015, MNRAS, 452, 1792